A 3D numerical simulation of different phases of friction stir welding

2009 Modelling Simul. Mater. Sci. Eng. 17 075001

(http://iopscience.iop.org/0965-0393/17/7/075001)

IOP PUBLISHING MODELLING AND SIMULATION IN MATERIALS SCIENCE AND ENGINEERING

Modelling Simul. Mater. Sci. Eng. **17** (2009) 075001 (32pp) doi:10.1088/0965-0393/17/7/075001

A 3D numerical simulation of different phases of friction stir welding

S Guerdoux and L Fourment

Mines ParisTech, CEMEF-Centre for Material Forming, CNRS UMR 7635, BP 207,
06904 Sophia Antipolis Cedex, France

E-mail: lionel.fourment@mines-paristech.fr

Received 23 September 2008, in final form 15 May 2009
Published 3 July 2009
Online at stacks.iop.org/MSMSE/17/075001

Abstract

An adaptive arbitrary Lagrangian–Eulerian formulation is developed to compute the material flow and the temperature evolution during the three phases of the friction stir welding (FSW) process. It follows a splitting approach: after the calculations of the velocity/pressure and temperature fields, the mesh velocity is derived from the domain boundary evolution and from an adaptive refinement criterion provided by error estimation, and finally state variables are remapped. In this way, the unilateral contact conditions between the plate and the tool are accurately taken into account, so allowing one to model various instabilities that may occur during the process, such as the role played by the plunge depth of the tool on the formations of flashes, the possible appearance of non-steady voids or tunnel holes and the influence of the threads on the material flow, the temperature field and the welding efforts. This formulation is implemented in the 3D Forge3 FE software with automatic remeshing. The non-steady phases of FSW can so be simulated, as well as the steady welding phase. The study of different process conditions shows that the main phenomena taking place during FSW can be simulated with the right sensitivities.

(Some figures in this article are in colour only in the electronic version)

1. Introduction

1.1. Friction stir welding

Since its invention in 1991 at TWI in England, the friction stir welding (FSW) process has enlarged the field of application of friction based technologies. FSW combines frictional heating and stirring motion to soften and mix the interface between two plates that are rigidly clamped and mated together (figure 1(*a*)), yielding a solid, fully consolidated weld. A rigid cylindrical spinning tool, composed of a protruding probe and a larger concentric shoulder, is

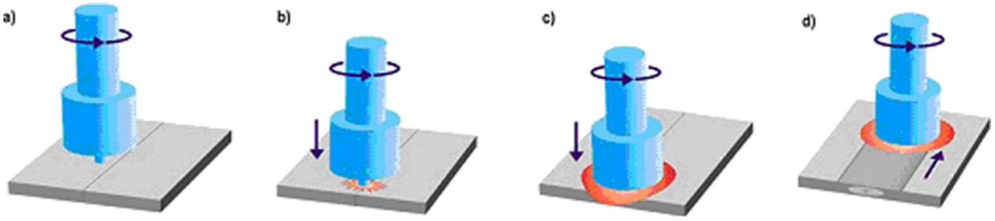

Figure 1. FSW phases: (*a*) initial, (*b*) plunging, (*c*) dwelling, (*d*) welding.

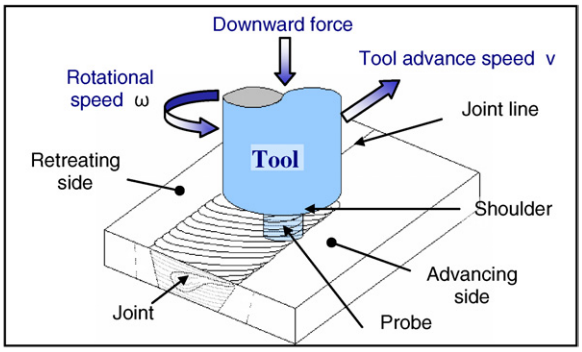

Figure 2. Welding phase and process parameters.

plunged into the joint line until the shoulder rests on the surface: this is the plunging phase (figure 1(*b*)). The dwelling phase (figure 1(*c*)) follows and rapidly softens the material through frictional heating. Then the tool is advanced along the joint line: the material is plastically deformed, stirred around the tool probe in a complex movement depending on forces involved and tool design (figure 1(*d*)).

The tool rotation rate (rpm) and the traverse speed ($\mathrm{mm\,min^{-1}}$) along the line of joint make up the two main parameters of the process (see figure 2). The rotation of the tool results in stirring and mixing, and its translation moves the material from the front to the back of the probe thus completing the welding process. Higher tool rotation rates generate higher temperatures and result in more intense stirring and mixing of the material. The insertion depth of the probe also plays an important role. When it is not enough, the tool shoulder does not correctly contact the original plate surface, so it cannot efficiently move the stirred material from the front to the back of the probe, resulting in welds with inner channels or surface grooves. When the insertion depth is too deep, the tool shoulder creates excessive flashes, a concave weld and a local thinning of the plates.

1.2. Numerical simulation of FSW

FSW being a still recent and complex process, sound welds are achieved only for specific combinations of parameters that have almost exclusively been obtained through extensive experiments, and the particular phenomena that are responsible for the material deposition are not fully understood yet. Numerical investigations have been much scarcely used for process set-up, although they can be helpful to better understand and observe the influence of input parameters on the resulting phenomena, to visualize and analyse the material flow, temperature map and strains.

The first models reported in the literature are analytical and address the temperature analysis. Initially based on Rosenthal's equations, they describe the quasi-steady temperature field of a semi-infinite body on which is applied a surface heat source moving with a constant velocity. The heat source really produced around the tool is replaced by simple analytical solutions [1]. McClure *et al* [2], along with Gould and Feng [3, 4], have incorporated in their equations the term of frictional heat, assuming a constant uniform pressure between the tool and the part. The traverse speed of the tool, the rotational velocity ω and the loading force F are the three parameters of the model. Schmidt *et al* [5] proposed an analytical expression of the estimated heat generation for more complex tool shapes. Thereafter, the convective heat transfer due to the material flow in the shear layer has been taken into account by prescribing a velocity boundary condition for the convective term in the energy equation. Khandkar *et al* [6] introduced a torque-based heat input model in which the local heat flux is linearly related to the distance to the tool axis. All these models constitute the first approaches to approximate the temperature map or the heat source in FSW. However, they are based on strong assumptions concerning the contact, by assuming pure sliding or sticking conditions, and always need the adjustment of experimental coefficients to be predictive. Moreover, they have low flexibility, as the tool design and the transient phases of the process are not taken into account, and they only provide temperature information. Their major interest is in feeding finite element (FE) solid-mechanics models with temperature fields.

When Lagrangian formulations are used, the high distortions of the mesh are the main difficulty that FE solid-mechanics models have to deal with. They occur under the tool shoulder, where high strains are logically observed during FSW, so the FSW tool is usually substituted by an analytical heat source. This approximation allows for computing the residual stresses that are due to thermal distortions, for instance as done by Chen and Kovacevic in the ANSYS code [7], where the heat source is assumed to be symmetric. Lawrjaniec *et al* [8] have developed two models using the thermo-mechanically coupled FE codes, SYSWELD and MARC. 2D surface heat sources, or 3D heat sources based on Russel's equations [9], are assumed to take into account the non-symmetrical character of the process. In the WELDSIM code, Chao *et al* [10] have modelled the mechanical actions of the tool at a uniform pressure. A Coulomb friction law is assumed and the frictional heat source due to the rotational movement of the tool is taken into account. However, none of these FE solid-mechanics based models are able to simulate the material flow.

The simulation of material flow during FSW has been logically modelled using computational fluid dynamics (CFD) formulations, the material being regarded as a viscous fluid flowing across a Eulerian mesh and interacting with a rotating tool. In the model developed by Ulysse [11], the contact is assumed to be sticking. Consequently, the heat source is only due to the viscous dissipation of the laminar flow [12]. Seidel and Reynolds [9] have approximated the viscosity by a function of the material yield stress throughout the Zener–Hollomon parameter. Their model has been implemented in the 3D code FLUENT. Colegrove *et al* [13, 14] have also used a CFD code to develop a global thermal model in which the heat flow, which is applied at the tool/workpiece interface, includes terms due to material shearing and friction. They have also developed a local model to visualize the influence of the screw on the material flow around the probe. In the approach of Dawson and co-workers [15], the evolution equation for strain hardening of the material is handled and integrated along the streamlines of the flow field, while various friction models for threaded tools are studied. The major weakness of these CFD like models is the approximations resulting from the material rheology, which generally does not allow for residual stresses prediction, and from the friction contact surface. In addition, the simulations of transient phases and defects of the process are hardly possible.

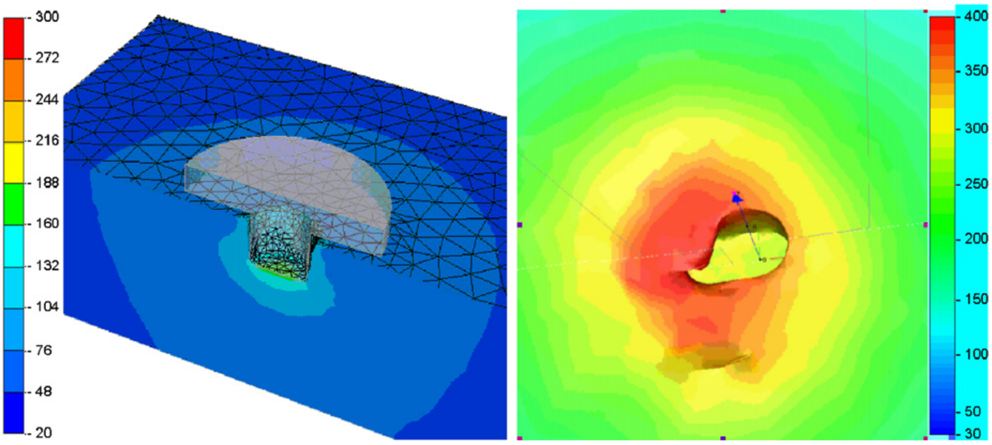

Figure 3. Numerical simulation of the plunging (left) and welding (right) phase with Forge3: isovalues of temperature (in °C).

In most utilized models, the contact conditions are enforced on the basis of an *a priori* knowledge of the process [16]. This prevents simulating the formation of voids that can occur under certain conditions. Very few models, like the one utilized by Schmidt and Hattel [17], actually take the unilateral contact conditions into account, and can be capable of predicting the process conditions that enable a successful material deposition. The model has been developed within the Abaqus Explicit software and utilizes an arbitrary Lagrangian–Eulerian (ALE) formulation. The remeshing algorithm provides an Eulerian character to the formulation that allows free surface movements to be modelled. The plunge phase is not simulated, but a spring force being applied to the tool, the initially prescribed plunge depth is automatically provided by the spring back of the tool, which settles at a value close to the experimentally observed one. The elasticity of the material is modelled by an elastic–plastic Johnson–Cook constitutive equation. The contact is bilateral during the period of time necessary to reach a steady state, and unilateral (so enabling void formation) afterwards, in order to verify that the material deposition process correctly occurs. A Coulomb friction law is assumed in this fully coupled 3D model.

The major difficulty of simulating the FSW transient phases consists of dealing with the large deformations taking place under the tool, while describing with enough accuracy any little surface movements in the contact area. When a Lagrangian description is utilized, the mesh is highly distorted, so remeshing is required almost continuously. This approach was followed by Fratini *et al* [18, 19] using the Deform software to simulate the welding phase. However, if it is desired to actually take into account the unilateral feature of the contact, this approach is not accurate. Figure 3 presents some preliminary results that have been obtained with the Forge3 software for the three FSW phases. During the plunging (figure 3—left), the numerical material is scarcely in contact with the vertical sides of the probe, which results in wrong temperature fields. They can be compared with more accurate results (see figure 13) in order to figure out the influence of the contact on the temperature profile. During the welding (figure 3—right), the material deposition does not properly occur at the back of the probe. It shows that the software is able to model voids formation but not to model sound welds.

A Eulerian like formulation more easily provides the history of the material flow during stationary welding, but the transient events, such as the phenomena of filling or of the prevailing cavity behind the probe of the tool, are hardly simulated because of the difficulty of tracking free surface movements. On the other hand, the ALE description makes it possible to take into account movements of free surfaces while reducing mesh distortions. This formulation procures the best compromise between Lagrangian and Eulerian formulations. Therefore, a 3D robust numerical tool enabling the thermo-mechanical simulation of the whole FSW process (plunging phase, dwelling phase and welding phase) has been developed, which makes it possible to better understand several FSW phenomena. After briefly presenting the developed adaptive ALE formulation, this paper focuses on the obtained results for several welding configurations.

2. Adaptive ALE formulation

For the simulation of both the quasi-Lagrangian plunging and quasi-Eulerian welding phases within a single numerical frame, an ALE formulation was developed into the Forge3 FE software [20, 21] by following a splitting method [22]. The treatment of the convective terms and the calculation of the mesh velocity being the two main difficulties of this approach, efforts have been made to improve the adaptive mesh velocity calculation [23] and the utilized remapping techniques [24].

2.1. Lagrangian step

Forge3 is extensively used to simulate hot, warm and cold forging of 3D geometry parts, using a pure Lagrangian formulation [20, 21]. At each time step, it solves the thermal and mechanical equations, which constitutes the first step of the implemented ALE splitting method [22]. The weak form of the momentum and incompressibility equations results in a mixed velocity–pressure formulation that is discretized by an enhanced (P1 + P1) quasi-linear interpolation based on four-noded tetrahedral elements. Viscoplastic, elasto-plastic and elasto-viscoplastic constitutive equations can be utilized to model the material deformations with elastic spring back and residual stresses. The contact is handled by a penalty formulation, and friction conditions at the interface between the part and the tools are modelled by Tresca, Coulomb or Norton laws. Furthermore, additional models can be introduced to more precisely describe the evolution of rheological and tribological parameters with temperature or any other internal variable. The discretized form of the heat equation is solved at each time step, and the coupling with the mechanical equations is done in an incremental way. The temperature evolution is also calculated in the FSW tool and the backing plate in order to better simulate the thermal boundary effects. Heat generated by material deformation and friction with the tool, thermal exchanges by conduction, convection and radiation are thus taken into account to model all welding phenomena.

2.2. ALE splitting formulation

The second step of the ALE splitting method consists of computing the mesh velocity, w, which can be different from the material one, v. It allows optimizing the elements quality and to increase the computation accuracy, independently from the material deformation. The final step of the method consists of dealing with the convective terms, which appear in the time grid derivatives of any variable φ through the following relationship:

$$\frac{\mathrm{d}_g\varphi}{\mathrm{d}t} = \dot{\varphi} + (\boldsymbol{w} - \boldsymbol{v}) \cdot \nabla\varphi, \tag{1}$$

where $\dot{\varphi}$ is the material derivative of φ.

2.3. Adaptive mesh velocity calculation

The mesh velocity $\boldsymbol{w}_n$ of any node n is calculated by an iterative centring algorithm. At any iteration it, equation (2) provides the new location of node n, while its grid velocity is deducted from equation (2) by equation (3).

$$\boldsymbol{x}_n^{\mathrm{it}} = \frac{1}{|\Gamma_n|}\sum_{e\in\Gamma_n} \boldsymbol{x}_{ge}^{\mathrm{it}-1} C_e^{\mathrm{it}-1}, \tag{2}$$

$$\boldsymbol{w}_n^{\mathrm{it}} = \frac{(\boldsymbol{x}_n^0 - \boldsymbol{x}_n^{\mathrm{it}})}{\Delta t}, \tag{3}$$

where Γ_n is the set of elements contiguous to node n (i.e. the set of elements which contain the node n, see figure 4), $\boldsymbol{x}_{ge}$ is the barycentre of element e. $C_e^{\mathrm{it}-1}$ is a weight factor that combines geometrical and adaptive considerations to provide fully regularized mesh with controlled elements qualities and optimized element size [23]. It is defined as

$$C_e^{\mathrm{it}-1} = (1 - \xi(\mathrm{Cf}_{\min}^{\mathrm{it}-1})) \times \mathrm{Cf}_e^{\mathrm{it}-1} + \xi(\mathrm{Cf}_{\min}^{\mathrm{it}-1}) \times \mathrm{Ca}_e^{\mathrm{it}-1} \tag{4}$$

with

$$\mathrm{Ca}_e^{\mathrm{it}-1} = \left(\frac{h_e^{\mathrm{opt}}}{h_e^{\mathrm{it}-1}}\right)^3 \qquad \text{and} \qquad \mathrm{Cf}_e^{\mathrm{it}-1} = \chi \frac{[V_e^{\mathrm{it}-1}]^+}{(p_e^{\mathrm{it}-1})^3}, \tag{5}$$

where V_e is the volume of element e, p_e is its perimeter. χ is an adimensioned constant such that Cf is equal to 1 for a perfect tetrahedron. ξ is a smoothed Heaviside function, such that $\xi(\mathrm{Cf})$ is equal to 0 if Cf is larger than the critical value $\mathrm{Cf}_{\mathrm{crit}}$ and else equal to 1 (with a smooth variation between 0 and 1). The optimal size h_e^{opt} of any element e (6) is calculated by a discretization error estimation in order to provide the best possible mesh for a given number of elements, Nbelt:

$$h_e^{\mathrm{opt}} = \left(\frac{\theta^{\mathrm{uni}}}{\theta_e}\right)^{2/(2p+3)} h_e \qquad \text{with } \theta^{\mathrm{uni}} = (\theta^{\mathrm{imp}})^{(2p+3)/2p}\left(\sum_e^{\mathrm{Nbelt}} (\theta_e)^{6/(2p+3)}\right)^{(2p+3)/4p} \tag{6}$$

where h_e is the present element size, θ^{imp} is the imposed value of the error and p is the convergence rate of the FE method (p is equal to 1 with the utilized P1 + P1 interpolation). θ_e is the contribution of element e to the estimated error in the energy norm (7), and θ^{imp} is computed (8) from the actual number of elements, Nbelt, in order to minimize the discretization error.

$$(\theta_e)^2 = \int_{\Omega_e} \mu(s_h)^{-1}(\tilde{s}_h - s_h) : (\tilde{s}_h - s_h)\,\mathrm{d}\omega, \tag{7}$$

where $\mu(s_h)$ is the equivalent material viscosity ($\dot{\varepsilon}_h = \mu(\boldsymbol{s}_h)^{-1}\boldsymbol{s}_h$, $\dot{\varepsilon}_h$ being the strain rate tensor), $\boldsymbol{s}_h$ is the deviatoric stress tensor ($\boldsymbol{s}_h = \boldsymbol{\sigma}_h + p_h\boldsymbol{I}$, where $\boldsymbol{\sigma}_h$ is the stress tensor and p_h the hydrostatic pressure) and $\tilde{s}_h$ is a recovered FE tensor, which is obtained using the patch recovery techniques based on recovery by equilibrium in patches [25] with some enhancements for boundary nodes [26].

$$\theta^{\mathrm{imp}} = (\mathrm{Nbelt})^{-p/3}\left(\sum_e^{\mathrm{Nbelt}} (\theta_e)^{6/(2p+3)}\right)^{(2p+3)/6}. \tag{8}$$

The calculation of the grid velocity w has to satisfy volume conservation conditions and more specifically to preserve the material flow through any part of the surface:

$$(\boldsymbol{w} - \boldsymbol{v}) \cdot \boldsymbol{n} = 0, \tag{9}$$

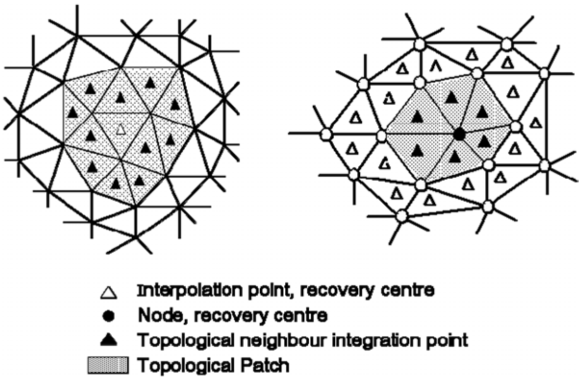

Figure 4. 2D illustration of element centred patches (left) and nodal centred patches (right).

where $\boldsymbol{n}$ is either a consistent normal to the workpiece on the free surface [22] or the outside contact normal. For points belonging to edges or similar zones, a local modal analysis allows selecting additional vectors to properly enforce the consistency condition in noticeable directions. Equation (9) is then enforced at any boundary node, for each selected normal directions, and its nodal $\boldsymbol{w}$ value is provided after these projections:

$$\boldsymbol{w} = \boldsymbol{w}^{\mathrm{it}} - \sum_{i=1}^{\mathrm{Nbdir}} ((\boldsymbol{v} - \boldsymbol{w}^{\mathrm{it}}) \cdot \boldsymbol{n}_i) \cdot \boldsymbol{n}_i. \tag{10}$$

In order to minimize the volume diffusion due to the difference between tangential grid and material velocities, an orthogonal projection procedure has been added; it is presented in [24].

2.4. Variable remapping

A Lagrangian like transport method has been preferred to tackle the convective terms. In order to ensure accurate remapping of piecewise discontinuous ($P0$) variables (stress field tensor $\boldsymbol{\sigma}_h$ and equivalent strain $\bar{\varepsilon}$) as well as nodal linear continuous ($P1$) variables (T temperature), a remapping technique derived from the Liska–Orkisz meshless finite differences method (MFDM) [28] and the super convergent patch recovery (SPR) technique [27] has been implemented. It consists of computing the gradient of the selected variable on element centred patches (for $P0$ variables) or on nodal centred patches (for $P1$ variables), as illustrated in 2D in figure 4. Considering the stress remapping, for example, a recovered continuous solution $\tilde{\boldsymbol{\sigma}}_h^k$ is constructed on element centred patches from the Lagrangian values that are known at the integration points. $\tilde{\boldsymbol{\sigma}}_h^k$ is locally approximated by a second order polynomial on each patch:

$$\tilde{\boldsymbol{\sigma}}_h^k(x, y, z) = \boldsymbol{P} \cdot \boldsymbol{a}^k \tag{11}$$

with

$$\begin{aligned} \boldsymbol{P} &= (1, x, y, z, x^2, y^2, z^2, xy, xz, yz), \\ \boldsymbol{a}^k &= (a_1^k, a_2^k, a_3^k, a_4^k, a_5^k, a_6^k, a_7^k, a_8^k, a_9^k, a_{10}^k)^t. \end{aligned} \tag{12}$$

The consistency of the remapping operator requires that $\tilde{\boldsymbol{\sigma}}_h^k$ is equal to $\boldsymbol{\sigma}_h^k$ at the centre of the patch. It results that $\boldsymbol{a}_1^k$ is equal to $\boldsymbol{\sigma}_h^k$. The other coefficients are determined by minimizing the following least square expression on each patch:

$$\Pi(\boldsymbol{a}^k) = \sum_{i=1}^{\mathrm{NG}} (\boldsymbol{\sigma}_h(i) - \tilde{\boldsymbol{\sigma}}_h^k(x_i, y_i, z_i))^2, \tag{13}$$

where NG is the number of integration points (or of nodes, in the case of nodal variables) of the patch and $\boldsymbol{\sigma}_h(i)$ is the value of $\boldsymbol{\sigma}_h$ at the integration point (x_i, y_i, z_i). If NG is not large enough to provide a well-conditioned system, the patch is either enlarged with second order neighbours (for $P0$ variables) or the polynomial order is reduced (for $P1$ variables). The remapped values at ALE integration points are then obtained by the inverse interpolation of (11), using the patch centred at the nearest Lagrangian integration point.

2.5. Space and time discretization steps

In the thermo-mechanically affected zone, where most of the phenomena take place, except thermal conduction and residual stress propagation, the elastic contribution of the material is totally negligible, so the elasto-viscoplastic model can be regarded as a rigid-viscoplastic model, and as the formulation is fully implicit, its accuracy is not directly affected by the possible loss of equilibrium of the stress tensor after remapping, or by using large time steps. However, the time step and element sizes directly affect the accuracy of the material flow, the free surface and contact area calculations. As the computational cost of non-steady FSW computations is high, it is necessary to determine the largest time steps and element sizes that make it possible to properly model the main features of the process. Therefore, several simulations with different values of these numerical coefficients have been carried out to determine them. Adaptive remeshing based on error estimation allows building an optimal mesh for a prescribed number of elements, i.e. for a prescribed cost. As the problem is highly coupled, if the mesh is adapted with sufficiently small elements for the mechanical resolution, then it is also well suited for the thermal resolution, and can properly discretize the gradients of both fields. From the process simulation point of view, the primary goal is to properly model the flow around the probe. Provided that the welding conditions are adequate, i.e. that the material temperature is high enough, the material should remain in contact with the probe while the tool is advancing, in contrast to what was obtained with a standard Lagrangian formulation, as was shown in figure 3. This must be satisfied whatever the formulation utilized, either of an Eulerian type with a fixed tool and the flow going through the material mesh, or of a Lagrangian type with a mobile tool moving through the material mesh. So, the total number of elements of the mesh and the time step size are adjusted by trial and error until the calculated free surface of the flow no longer changes when these parameters are reduced.

3. Process modelling

3.1. Process geometry

The tool used for this study was manufactured from heat-treated H13 tool steel. Its dimensions consisted of a shoulder diameter of 25.4 mm, body length (from the top of the tool to the shoulder) of 83.8 mm and shoulder concavity angle of 8° (see figure 5). The probe is 6.35 mm long and is unthreaded. The tool was used at a tilt angle of 2.5°. Its FE discretization can be seen in figure 5.

The aluminium plate is made of Al 6061 with a thickness of 9.53 mm. As it is very large, in the FE model its dimensions are reduced to a width of 150 mm and a length of 300 mm. It is assumed that the distance from the tool to the edges is large enough to allow proper computations of the thermal fields at steady state. The backing plate is also modelled with the same dimensions as the workpiece and a thickness of 25 mm, as presented in figure 6.

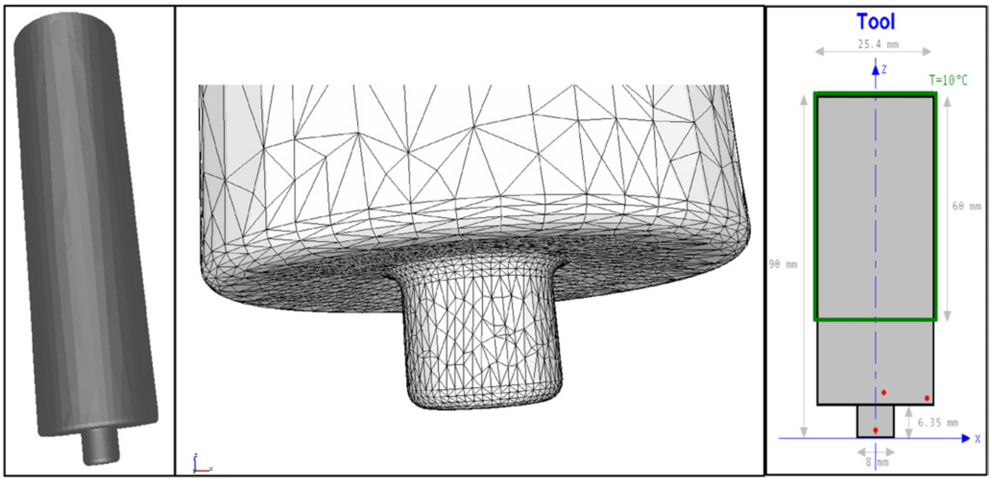

Figure 5. Global view of the tool, its dimensions and local view of its mesh.

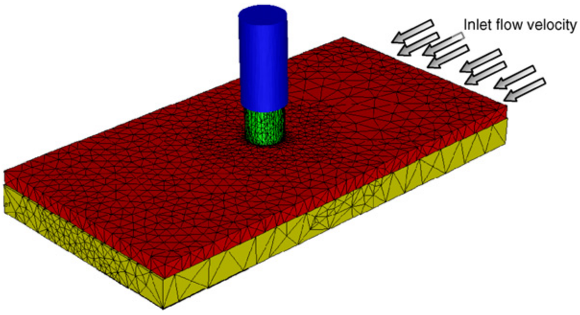

Figure 6. Global view of the FE process modelling.

3.2. Material models

Most material models utilized in the Forge3 FE software are based on the Hansel–Spittel constitutive equations:

$$\bar{\sigma} = \sigma_f = A_1 \exp(m_1 T)\, \bar{\varepsilon}^{m_2}\, \dot{\bar{\varepsilon}}^{m_3} \exp\left(\frac{m_4}{\bar{\varepsilon}}\right), \tag{14}$$

with

$$\bar{\sigma} = \sigma_f = \sqrt{\frac{3}{2} s : s}, \qquad \dot{\bar{\varepsilon}} = \sqrt{\frac{2}{3} \dot{\varepsilon}_{\mathrm{vp}} : \dot{\varepsilon}_{\mathrm{vp}}}, \qquad \bar{\varepsilon} = \int_0^t \dot{\bar{\varepsilon}}\, \mathrm{d}t, \tag{15}$$

where $\bar{\sigma}$ is the equivalent stress, $\dot{\bar{\varepsilon}}$ is the equivalent strain rate with $\dot{\varepsilon}_{\mathrm{vp}}$ the viscoplastic component of the strain rate tensor, $\bar{\varepsilon}$ is the equivalent strain and A_1, m_1, m_2, m_3, m_4 are the model coefficients.

The Forge3 material database provides two different Hansel–Spittel laws (see table 1) for the constitutive behaviour of the Al 6061 material, whose solidus and liquidus temperatures, respectively, are around 582 and 652 °C. The first law is elasto-viscoplastic; it is advised for a temperature range of 20–250 °C. The second law is purely viscoplastic; it is recommended for a temperature range of 250–550 °C.

Table 1. Hansel–Spittel coefficients for AlMgSiO, 6Cr (DIN)-6061 (US).

	Cold law	Hot law
Temperature range (°C)	20–50	250–550
Strain range	0.04–3.0	0.04–1.5
Strain rate range (s^{-1})	0–500	0–300
A_1 (MPa)	260.5	352.4
m_1	−0.0017	−0.0045
m_2	0.17	0.066
m_3	0.018	0.13
m_4	−0.00073	0.0024

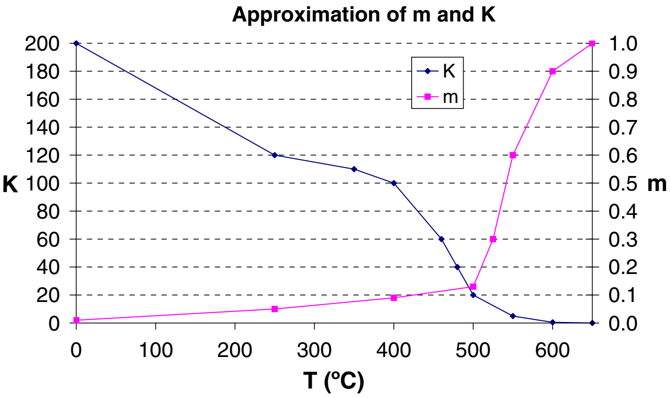

Figure 7. Tabulated values of the material consistency K and its strain rate sensitivity m as functions of temperature.

However, the two laws do not perfectly meet around 250 °C, and the hot law results in material temperatures that can reach the melting point during the process simulation, which exceeds its validity limit. On the other hand, the behaviour of the material is expected to change rapidly in the highly thermally affected zones, which is difficult to model with these laws. In order to derive a single constitutive model for the whole range of temperatures and to take these constraints into account, the material consistency K and the strain rate sensitivity m have been tabulated as functions of temperature, as presented in figure 7, while strain hardening was neglected. The resulting constitutive equation is written as

$$\bar{\sigma} = \sigma_f = K(T)(\sqrt{3}\dot{\bar{\varepsilon}})^{m(T)}. \tag{16}$$

The resulting law is visualized in figures 8 and 9. It provides a good approximation of the Hansel–Spittel constitutive models of Al 6061 under hot and cold conditions, as well as consistent values in the process variation domain of strain rates and temperatures. It will be used in all the forthcoming simulations with any aluminium material, even with the Al 7035, in the absence of sufficiently precise data to make the difference between the two materials. The elasto-plastic behaviour of the material at cold temperatures is also taken into account, with a Young's modulus that is equal to 73 GPa and a Poisson's coefficient that is equal to 0.3.

The thermal characteristics of the Al 6061 workpiece, H13 tool and the backing plate are assumed constant. They are summarized in table 2.

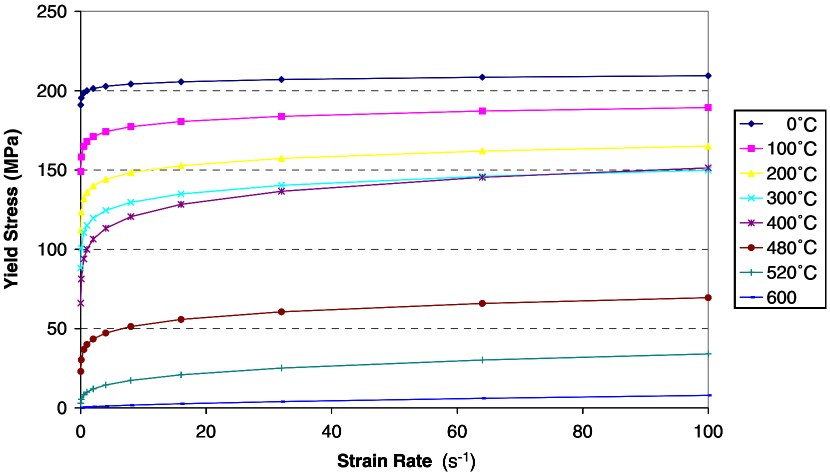

Figure 8. Yield stress (MPa) as a function of equivalent strain rate (s^{-1}) for different values of temperature (°C), with the tabulated law.

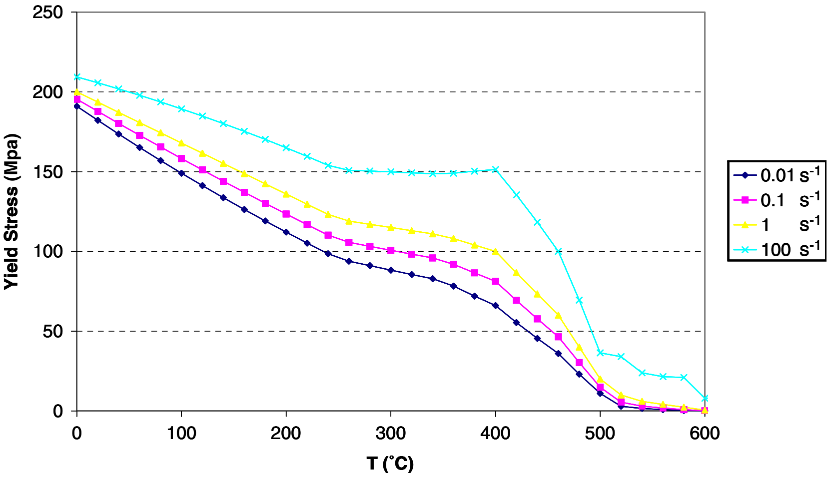

Figure 9. Yield stress (MPa) as a function of temperature (°C) for different equivalent strain rate values (s^{-1}), with the tabulated law.

Table 2. Thermal characteristics of the modelled materials.

	Conductivity, λ ($W\,m^{-1}\,{}^{\circ}C^{-1}$)	Thermal capacity, c ($J\,kg^{-1}\,{}^{\circ}C^{-1}$)	Density, ρ ($kg\,m^{-3}$)	Effusivity, $E = \sqrt{\lambda\rho c}$ ($J\,kg^{-1}\,m^{-3}$) ($m^{-2}\,s^{-1}$)	Emissivity
Workpiece Al 6061	180	896	2 700	20 868	0.05
FSW Tool H13	24.3	460	7 850	9 367	0.88
Backing plate	250	1 230	2 800	29 343	0.05

Table 3. Thermal boundary conditions of the model.

Thermal exchange coefficients h_c between ↓ and →	FSW Tool H13	Anvil backing plate	Tool holder (15 °C)	Rigid cooling plate (15 °C)	Ambient air (20 °C)
Workpiece Al 7075	50 000	2 000	—	—	30
FSW Tool H13	—	—	20 000	—	20
Anvil backing plate	—	—	—	2 000	30

3.3. Boundary conditions

During dwelling and welding, the spindle speed is set to 650 rpm. During welding, the transverse velocity of 3.39 mm s^{-1} is prescribed as an inflow velocity at the nodes of the upwind side of the plate (see figure 6), with a constant temperature of 20 °C. The tool and the tool holder have a rigid body movement. During the welding phase, the tool quickly reaches a steady-state temperature that is close to the plate temperature, which consequently results in a poor thermal exchange between them. The different utilized thermal exchange coefficients and the prescribed temperatures for bodies are assumed constant and summarized in table 3.

At the interface between the plate and the tool the friction is supposed to obey the Norton law:

$$\boldsymbol{\tau}_f = -\alpha_f K(T)||\boldsymbol{\Delta v}_s||^{p-1}\boldsymbol{\Delta v}_s \tag{17}$$

with

$$\boldsymbol{\tau}_f = \boldsymbol{\sigma}\cdot\boldsymbol{n} - \sigma_n\cdot\boldsymbol{n} \qquad \text{and} \qquad \Delta\boldsymbol{v}_s = (\boldsymbol{v}-\boldsymbol{v}^{\text{tool}}) - [(\boldsymbol{v}-\boldsymbol{v}^{\text{tool}})\cdot\boldsymbol{n}]\boldsymbol{n}, \tag{18}$$

where α_f and p are the friction coefficients, $\boldsymbol{n}$ is the outside normal, $\sigma_n = (\boldsymbol{\sigma}\cdot\boldsymbol{n})\cdot\boldsymbol{n}$ is the normal stress and $\boldsymbol{v}^{\text{tool}}$ is the contacting tool velocity.

3.4. Friction calibration

The accurate modelling of friction constitutes a key point of FSW simulation. In fact, the contact features strongly depend on the process conditions, because any material point of the surface located under the tool shoulder can either be in contact and rubbing, or not be in contact and not rubbing, according to the computed material flow (in other words to the solution of the thermo-mechanical computations), while the friction model determines the shear stress at the contact interface and consequently the material warming up, the resulting viscosity and finally the material flow. In a first approach, the friction was calibrated with respect to the integrated mechanical values, torques and forces. The numerical simulation of the welding phase was then carried out in the proposed configuration, using three sets of friction coefficients: (1) $\alpha_f = 0.3$, $p = 0.125$, (2) $\alpha_f = 0.4$, $p = 0.10$ and (3) $\alpha_f = 0.4$, $p = 0.125$.

As torques were not directly available from the experiments, the motor power values were compared. This is the amount of power required by the welder to turn the spindle under the load, which includes the power required to overcome frictional losses. In a separate experiment, the free-wheel power required by the spindle motor at various spindle speeds was measured to approximate the motor losses. This value was then subtracted from the steady-state averaged motor power values of the welding experiments. The resulting value is compared in figure 10 with the calculated values for the three frictional cases. It shows that the equivalent power, which is the product of the axial torque with the spindle speed, is not very sensitive to the variations of friction. As a matter of fact, it is not a proper value for parameter identification. On the other hand, the values of the equivalent motor power appear to be quite noisy and

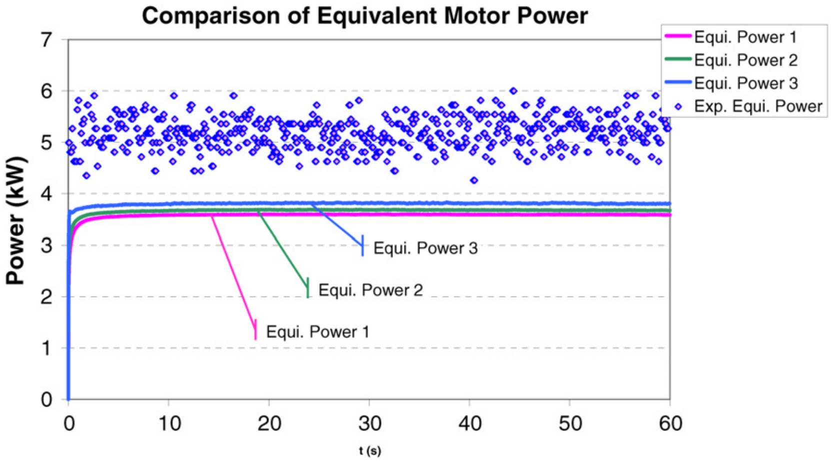

Figure 10. Comparison of an estimation of the experimentally measured motor power with the calculated values in the three studied cases: (1) $\alpha_f = 0.3$, $p = 0.125$, (2) $\alpha_f = 0.4$, $p = 0.10$ and (3) $\alpha_f = 0.4$, $p = 0.125$.

scattered. In spite of the introduced correction, the measured values are much larger than the calculated ones. It is likely that the losses which occur during welding are larger than during a free-wheel state because of the increased strain on the gears and bearings. It is recognized that the free-wheel power measurements are a lower limit of these losses. Therefore, it can only be concluded that the simulated values provide a good order of magnitude and the difference between the values has the right sign.

On the other hand, figure 11 shows the sensitivity of both the F_z (in the axial direction) and F_x (in the transverse direction) forces to friction. The obtained values are very sensitive to the friction parameters; they vary with a very large ratio that is close to 2. Therefore, this experiment allows carrying out a satisfactory parameter calibration. Figure 11 also shows that a very good agreement is obtained with the third set of coefficients, $\alpha_f = 0.4$ and $p = 0.125$, for both the vertical and the horizontal forces. The gap between the curves is included in the experimental and numerical errors.

3.5. Threads model

In order to model the influence of threads in a simple way, the actual shape of the thread is not taken into account since it would require excessively fine meshes and result in very frequent element distortions. Therefore, the shape of the probe is kept perfectly cylindrical and the threads are simply modelled by their resulting action, a virtual axial velocity V_{screw} along the probe, which is added to the rotational velocity ω_{tool}. Therefore, this additional term is introduced in equation (18) in the friction analysis with the lateral faces of the probe. This resulting axial velocity can be correlated with the equivalent pitch of the screw, p_{screw}, and to the tool rotating velocity ω_{tool}, as presented in equation (19) and illustrated in figure 12. Further improvements would consist of taking into account the threads angle and an additional velocity component in the θ direction (tangential to the probe and perpendicular to the rotation axis) as in [15] for instance.

$$V_{\text{screw}} = 2\pi\,\omega_{\text{tool}}\,p_{\text{screw}}. \tag{19}$$

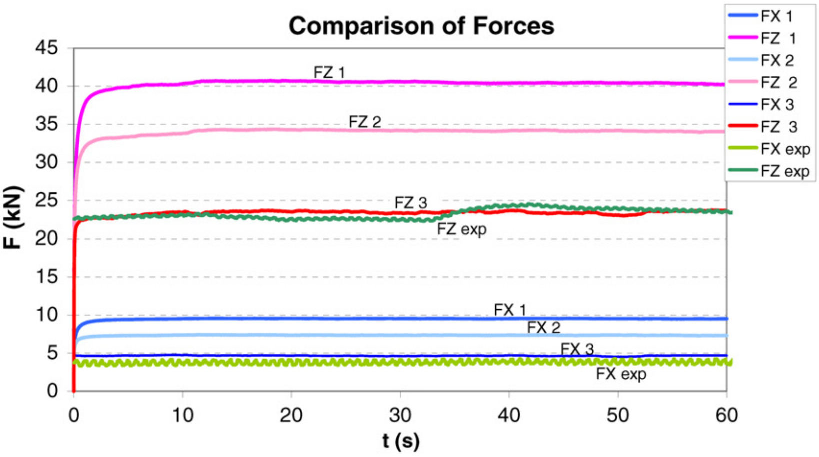

Figure 11. Comparison of experimentally measured horizontal (F_x) and vertical (F_z) forces, with the calculated ones in the three studied cases: (1) $\alpha_f = 0.3$, $p = 0.125$, (2) $\alpha_f = 0.4$, $p = 0.10$ and (3) $\alpha_f = 0.4$, $p = 0.125$.

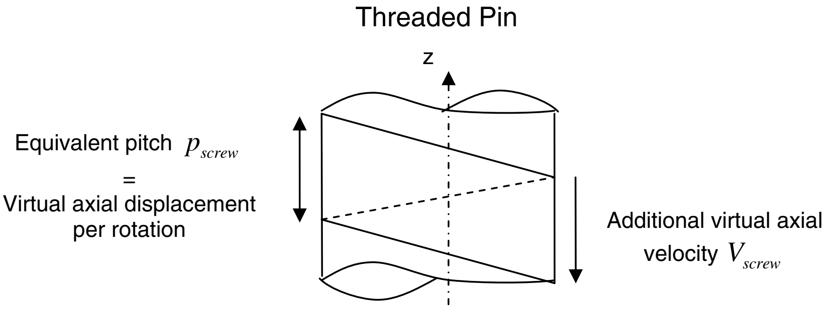

Figure 12. Illustration of the additional virtual axial velocity for modelling the influence of the threads.

4. Plunging simulation

Often ignored in the literature, the simulation of the transient states of the FSW process is enabled with the developed ALE formulation. Therefore, a specific section is dedicated to the study of the plunging phase, which can be regarded as a separate experiment to calibrate some of the material and interface coefficients, or as a preliminary study towards the simulation of friction stir spot welding, which derives from FSW in the sense that the two stacked parts are welded together by several plunging and dwelling phases. Consequently, the tool was not tilted (whereas there is a tilt of 2.5° in all the other simulations); its rotational speed was 600 rpm (instead of 650 rpm in all the other simulations); the plate thickness was 19.1 mm (instead of 9.53 mm in all the other simulations) and the plunging depth was much deeper than the value that will be considered for welding. As in the other experiments and simulations, the plunge rate was $1.19\,\mathrm{mm\,s^{-1}}$.

Since the contact conditions are not prescribed, partial contact is allowed at the tool/matrix interface, e.g. at the periphery of the shoulder and the probe, where a ‘foot print’ dependent solution is calculated. Since the temperature distribution within and around the stirred zone directly influences the microstructure of the welds, such as the grain size, the coarsening and dissolution of precipitates and the resultant mechanical properties of the welds, it is again of major importance to accurately compute the temperature distribution. At the end of plunging, the temperature field usually provides the initial state of the welding phase and makes it possible to correctly predict the transient conditions of the initial deposition process at the back of the probe. The beginning of plunging results in intense friction between the tip of the probe and the workpiece. Heating increases as the friction area enlarges on the lateral face of the probe. Before the shoulder comes into contact, the plastic deformation is mainly due to the indentation of the tool. Then the intense friction and plastic deformations around the rotating tool are the two factors which contribute to the temperature increase within and around the stirred zone. The evolution of the temperature field in the cutting joint during the 7 s simulation is shown in figure 13.

The experimentally obtained profile of the thermally affected zone (TAZ) (see top of figure 14) extends from the edge of the shoulder, down underneath the probe tip and back to the edge of the shoulder on the opposite side of the probe. It provides a physical indication of the isotherms taking place during the plunging sequence, and a comparison with numerical results is proposed in the left part of figure 14. The temperature provided by the simulation between the two red lines ranges from 250 to 370 °C. The material located above this second red line has reached the annealing temperature, which is about 413 °C for the Al 7035 used in the experiment. In the mechanically affected zone (MAZ), the solidus temperature of 477 °C is reached. The equivalent strain field obtained at 5.4 s from the simulation is shown in the right part of figure 14. It is noticed that the equivalent strain ranges between 2% and 5% in the experimentally observed MAZ. This value quickly increases when the shoulder is maintained in contact, and a value of about 10% is reached in the MAZ at $t = 6$ s.

5. FSW simulation: simulation of the three stages of the process

The three welding operations, plunging, dwelling and welding, are successively simulated according to the process parameters presented in section 3. It shows the capacities of the software to handle these three very different types of flows, but also and above all, the feasibility of the weld under these process conditions, from the beginning to the steady state. Figure 15 presents the temperature fields inside the tool, the workpiece and the backing plate in the cross joint section for the plunging phase, after the dwelling phase and at transient welding time. During the 15 s of the plunging step, the temperature evolution is quite similar to that of the previous section, except that the tool tilt introduces a slight dissymmetry in the temperature field and in the roll of material on the free surface (figure 15(*c*)). The temperature suddenly increases at two occasions, when the tool shoulder comes into contact with the plate (figure 15(*d*)) and later when the tool starts moving forwards (figure 15(*f*)). With respect to the previous section, the tool is not plunging as deep. Its penetration into the plate is a crucial parameter for the material flow and for the formation of flash like small surface defects around the tool shoulder. The temperature continues to increase during the dwelling phase (figure 15(*e*)), in both the material and the tool, until it reaches a proper welding temperature. A very small cavity also starts forming at the bottom of the probe, but when the tool starts moving forwards, the temperature increases further and the cavity disappears (figure 15(*f*)). The tool absorbs a large amount of generated heat. After the non-steady stages of plunging and dwelling, it rapidly reaches a steady temperature distribution (figure 15(*f*)). The highest temperatures are observed on the tool shoulder, closely followed by the value at the probe tip. The temperature of the backing plate poorly increases, so its evolution cannot be properly

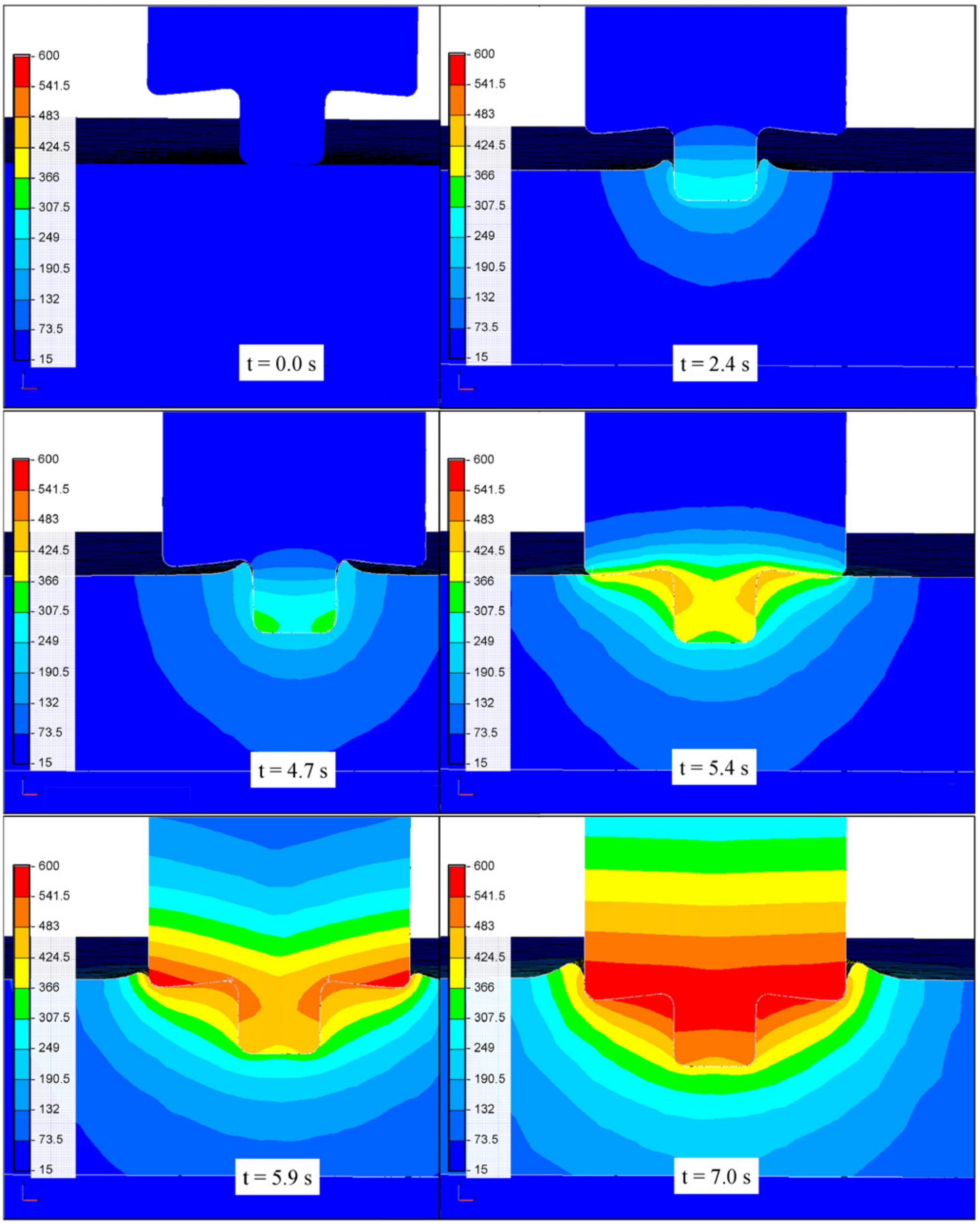

Figure 13. Temperature map (in °C) in the cutting joint plane during the plunging phase; the tool is untilted and unthreaded.

observed in the pictures of figure 15. The reader is invited to look at figure 16 where this temperature change can be better seen.

Free surface movements still being allowed during the welding stage, the friction area is not constant and strongly depends on the plunge depth of the tool, until the steady state is reached (figure 15(*f*)). Figure 16 shows the temperature map in the cross joint section after 13 s of welding and the corresponding friction interface. It is noticed that the shoulder is not fully in contact with the workpiece, which would not be the case with an Eulerian formulation.

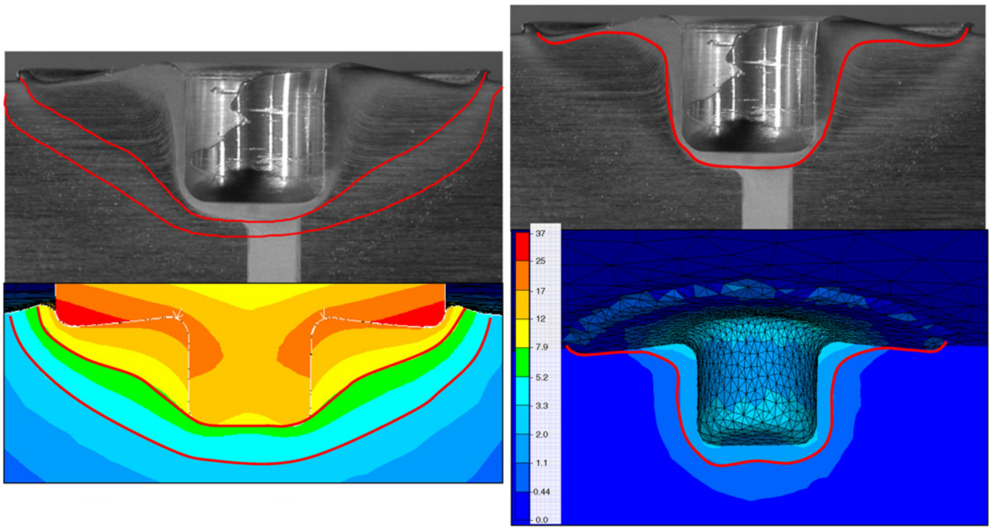

Figure 14. Comparisons between the microstructure observations in the cross section and the calculated fields. Left: comparison between the experimentally observed TAZ and the simulated temperature field (in °C). Right: comparison between the experimentally observed MAZ and the simulated equivalent strain field when the shoulder is just getting in contact with the plate ($t = 5.4$ s).

For comparison with Eulerian approaches found in the literature, the same simulation is carried out within an Eulerian frame: the free surface is assumed to remain constant after the plunge and the shoulder is considered as fully in contact with the plate. The heat generated by friction is then larger than in the ALE simulation. The material is more softened and the resulting forces are a little lower. Forces and torques simulated in the Eulerian and ALE frameworks are compared in figure 17. The calculated torques are similar, but there is a difference of about 30% on the horizontal and vertical forces, which is in agreement with results of section 3.4 where it was noticed that torque is much less sensitive than forces to friction.

It is also noticed that some nodes located at the bottom trailing side of the probe appear in dark (blue) in figure 16, which means that they are not in contact. It reveals that either the friction coefficient is close to being under-evaluated, or that the welding configuration is close to the limits of a good deposition process. However, although these nodes are not always in contact with the probe, the created little gap is automatically filled while the probe moves along the joint line, and no tunnel hole is formed.

During the dwelling phase, a temperature drop takes place just before the beginning of the welding phase. It results from the reduction in the contact area, which is induced by the stopping of the translational movements of the tool and the consequent decrease in the vertical forces. It correlates well with the experimental observations that are usually made when the vertical position of the tool is controlled by position and not by force. For a more precise study of this feature, the dwelling simulation is carried out again with a small constant plunge velocity of 0.05 mm s^{-1}, which ensures an almost constant vertical force. Figures 18 and 19 show the differences that are respectively observed on the temperature fields (top surface of the workpiece and cross section views) and on the forces and torques during the two 2.5 s dwelling simulations. In the 'force controlled' simulation, the load logically increases and consequently the heat produced by friction. On the other hand, the original simulation provides consistent

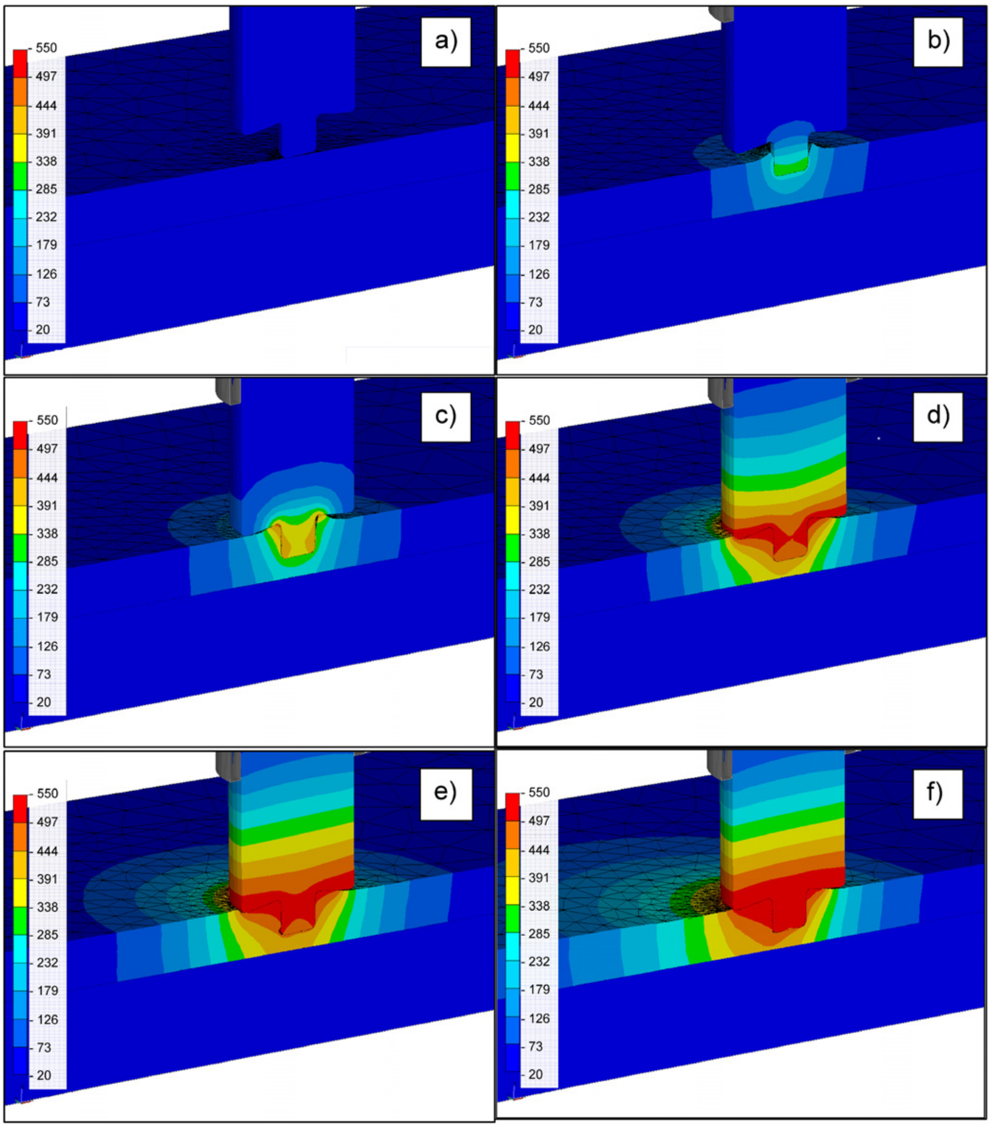

Figure 15. Temperature field (in °C) during transient states of the process (cross section view): (*a*) initial state, (*b*) and (*c*) plunging phase, (*d*) end of the plunging phase, (*e*) after dwelling phase, (*f*) transient welding phase.

results: in the beginning, the plunge force and torque rapidly decrease, then stabilize and finally slowly decrease as the temperature of the workpiece globally increases.

6. Numerical model capabilities

The purpose of this work is to develop an adaptive ALE formulation that makes it possible to simulate the FSW process and to compute its thermo-mechanical fields with precision. It does not pretend, however, to be a predictive model, because predictability requires not only

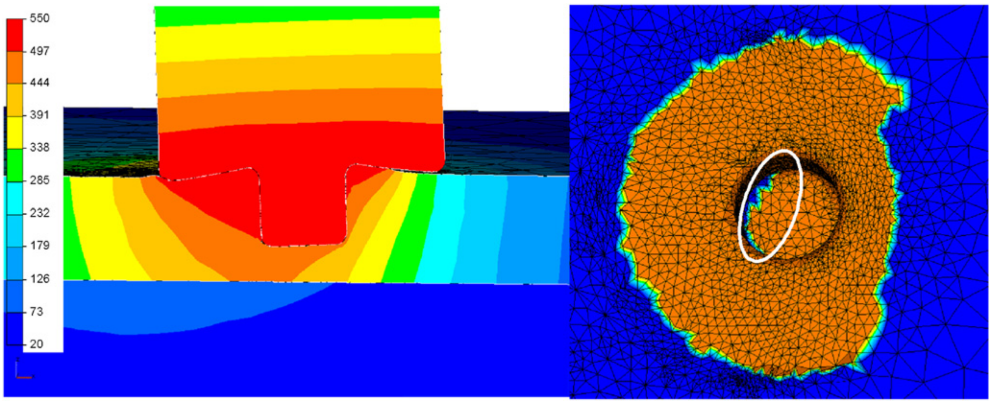

Figure 16. Temperature field (in °C) obtained after 13 s of welding with ALE formulation in the cutting joint plan (on left side) and top view of the friction area at the same time (on right side): dark (blue) nodes are not in contact.

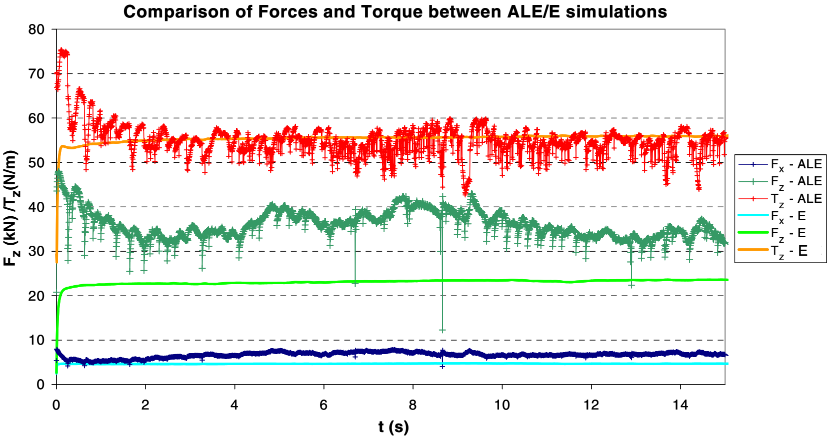

Figure 17. Comparison of the welding forces and torques resulting either from an Eulerian or an ALE simulation.

accurate and robust software but also accurate and reliable models for the material, friction and interface behaviour, which is far beyond the objectives of this paper, due to the complexity of this problem. Therefore, this section only aims at verifying whether this formulation has the capabilities to simulate the main phenomena that are observed in FSW, whether it properly reproduces the right tendencies and sensitivities of the process and whether it is sufficiently general to apply to the various configurations of FSW.

6.1. Defects formation

In order to simulate any possible defect that might take place during the welding process, the adaptive ALE formulation is expected to simulate any small movements of the free surface of the plate. A judicious choice of the time step (it has to be small enough, ranging between 8×10^{-4} s and 2×10^{-3} s), combined with a tool smoothing procedure and the mesh adaptation procedure, has made it possible to reach the required accuracy. During plunging and welding,

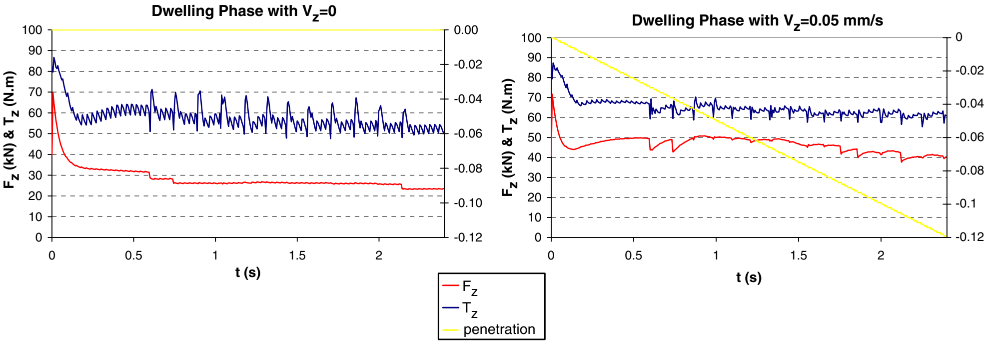

Figure 18. Comparison of vertical forces (F_z) and torques (T_z) observed during the dwelling phase simulation with (on right) and without (on left) low plunge velocity.

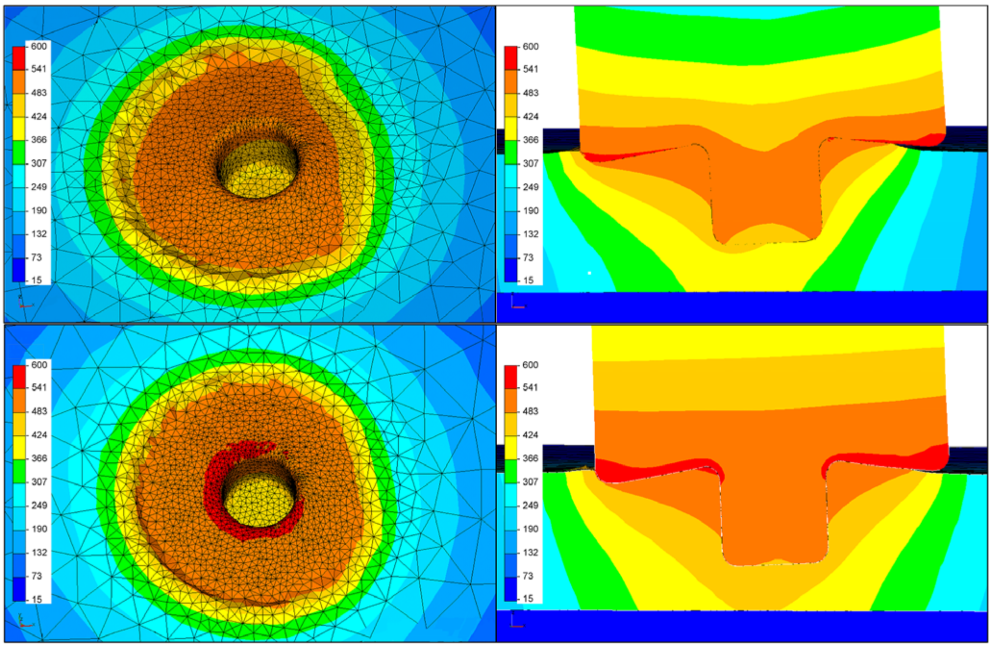

Figure 19. Comparison of the temperature field (in °C) observed after 2.5 s of dwelling phase simulation with (bottom) and without (on top) low plunge velocity.

a significant amount of flash is generated, which curls up from beneath the tool (see figure 20). The deeper the tool penetration into the plate is, the larger the volume of the flash. Figure 21 shows the ability of the numerical model to simulate such details of the process and render the flash formation.

However, the computational cost for the simulation of these details is very high, as they require very fine meshes to model the flashes, whereas they do not play a significant role on the quality of the weld. On the other hand, the plunge depth of the tool into the workpiece cannot be artificially modified, because it influences the friction area and so loads and temperature of the process. Therefore, it is decided to change the type of formulation according to the different zones of the plate, in order to fit it with the level of details that are expected from the simulation.

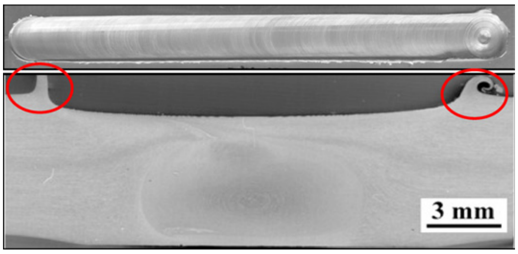

Figure 20. Experimental flash formation during welding (top view and transverse cross section) of aluminium under standard welding conditions.

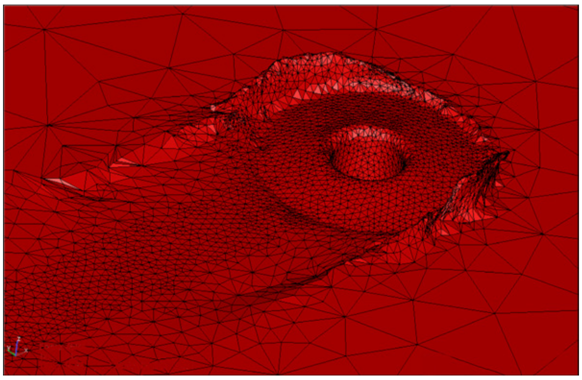

Figure 21. Example of flash occurring during an ALE simulation of transient welding phase.

A local Eulerian description is then used in the flash zone, while an ALE description is kept everywhere else. This way, the model is accurate enough to take into account possible void formations at the back of the probe, but not to simulate minor phenomena like flash formations at the shoulder periphery.

One of the main advantages of the proposed description is the possibility of predicting void formation. The ALE formulation actually allows the separation between the workpiece and the tool. Figure 22 shows an example of a non-successful deposition in which a void is formed at the lower advancing trailing side of the probe/matrix interface. It is to be noticed that the voids actually form on the advancing side, as in the actual process for a large range of alloys. According to the process conditions, some voids may form periodically, while some others may result in so-called 'tunnel holes' or else disappear while a stable deposition process takes place. This cross section view also shows that the void tends to be partially filled during the process. The same mechanism is also depicted in figure 23, but in this case the tendency of the void to disappear is clearer. This capacity of simulating voids is actually very important because there is no other satisfactory way to model these types of defects: within an Eulerian frame, some of the other approaches are based on a damage criterion or the analysis of the stress components, which do not make it possible to indicate whether a void is formed or about to be formed and so to model non-steady voids.

6.2. *Threads sensitivity*

The tool design plays a very important role in the production of successful joints by FSW. The tool shape and size dictate, to some degree, the material flow and heat generation in the

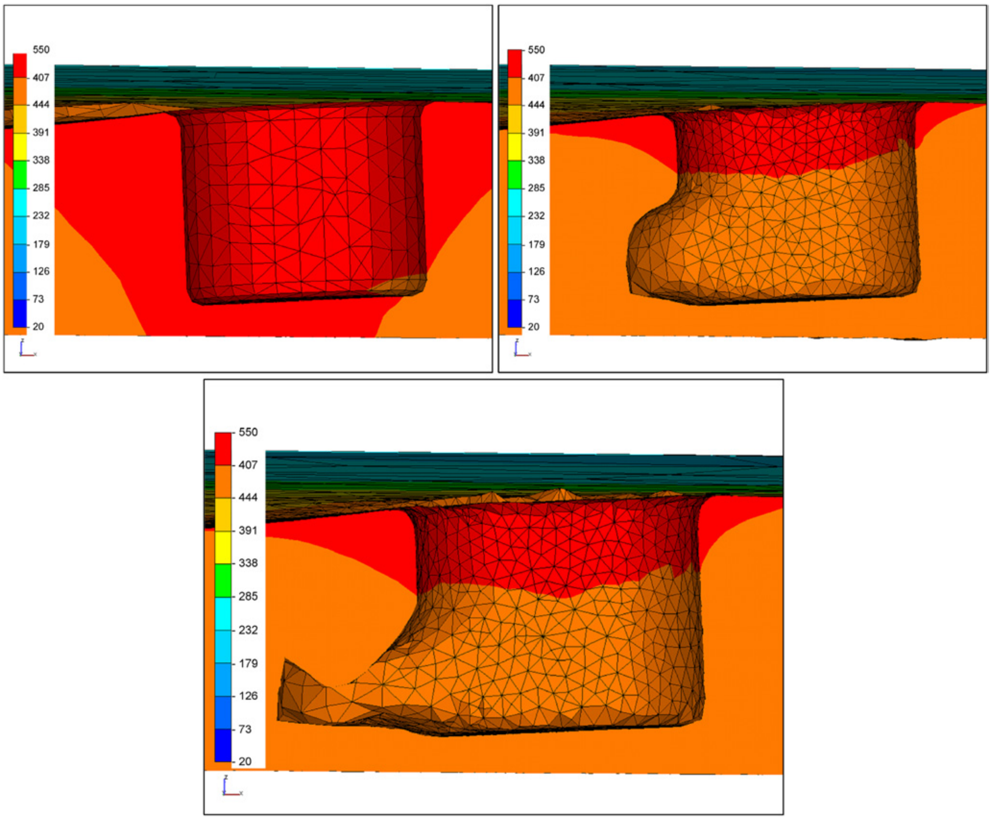

Figure 22. Void formation at the back of the probe (cross section view) at $t = 0$ s, $t = 2.5$ s, $t = 5$ s with temperature isovalues (in °C).

weld zone, which in turn, affect the weld final properties. The simulation provides information which can be helpful for tooling design. This section investigates the influence of threads on the probe, with 2 and 10 mm equivalent pitch. The simulations have been run keeping the same thermal, mechanical and process parameters. Figure 24 presents the temperature maps in the cross section in the 2 mm pitch case, showing an increase in the temperature at the contacting lateral sides of the probe with respect to the case without threads.

This tendency is confirmed in figure 25, with the temperatures at the three tool sensors locations (tip of probe, root and shoulder). A simulation with a 10 mm equivalent screw pitch has also been carried out, whose results clearly demonstrate the influence of threads on the temperature increase in the probe.

Figure 26 shows that the torque consequently decreased with threaded probe, while the axial load (see figure 27) is nearly the same in both the configurations, with and without threads. With the threaded probe, the increased heating of the material might result in a lower welding force, but it is compensated by the vertical reaction force that is generated by the threads. The traverse force is also lower in the case of the threaded probe, which is observed in the experiments.

Figure 28 shows that the threads also have an effect on the equivalent strain map: the strain is higher and less concentrated at the root of the probe when the latter is threaded.

In practice, threads are introduced to modify the flow by pushing down the material along the probe in order to avoid the formation of voids. A new complete ALE simulation, from the

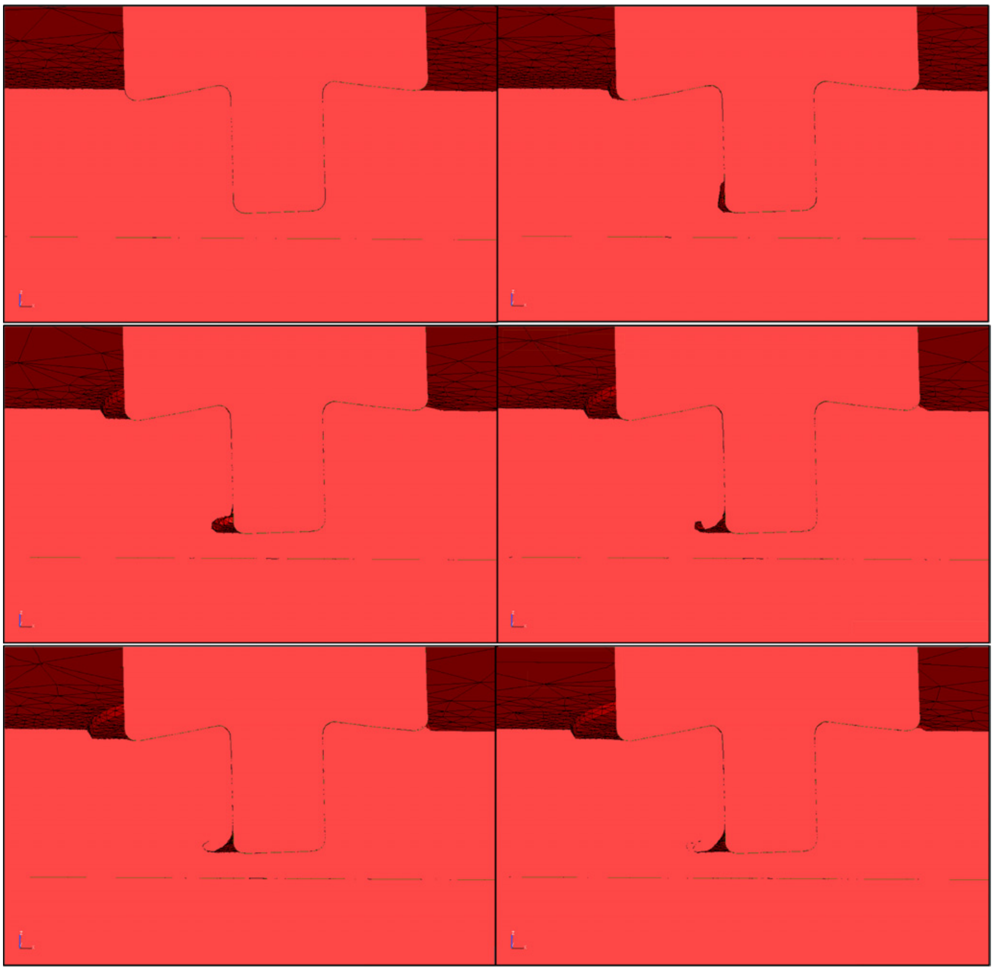

Figure 23. Initial void formation on the trailing edge of the probe due to bad initial process conditions (cross section view), which tends to disappear as the process goes on.

transient to the steady welding state, has been carried out with the same model parameters and a 10 mm equivalent screw pitch. Figure 29 shows the observed differences in the temperature field in the cross joint section and in the equivalent strain in a transverse cross section just behind the probe, after 21 s of welding. The modelled threads clearly increase the temperature along the probe and change the material flow. These result in more concentrated high equivalent strain at the bottom of the probe, where the so-called nugget zone clearly appears. Last and not least, the losses of contact, which appear at the bottom trailing edge of the probe (see figure 16) in the case without threads, are no longer observed with the modelled threads, which numerically confirms the role played by the threads in FSW.

In order to visualize the material flow for both the simulation cases, the stream lines of 78 material points have been plotted in figure 30. These trajectories have been computed backwards, by going back up the flow, for uniformly distributed points at the exit of the plate. It is very clear that the material flow within the nugget consists of several independent deformation processes. In the case with threads, the material particles are quickly dragged from the top surface to the bottom; the particles close to the top surface are less trapped under the

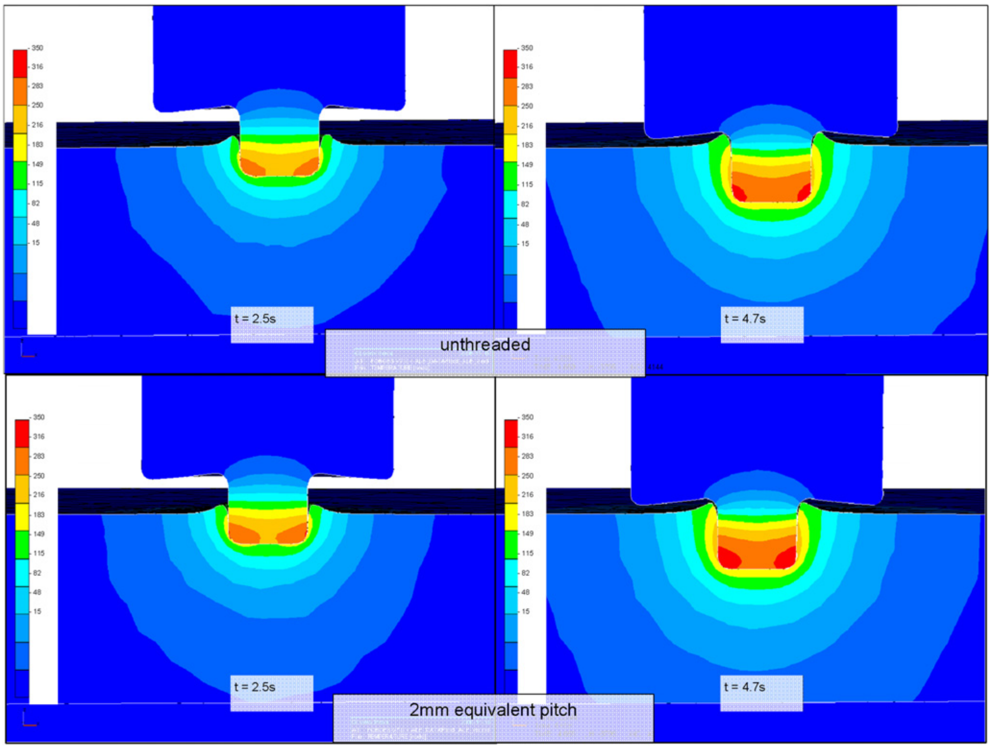

Figure 24. Comparison of temperature maps (in °C) in the cross section during the plunging phase without (top) and with (bottom) threads for a screwed probe of 2 mm equivalent pitch.

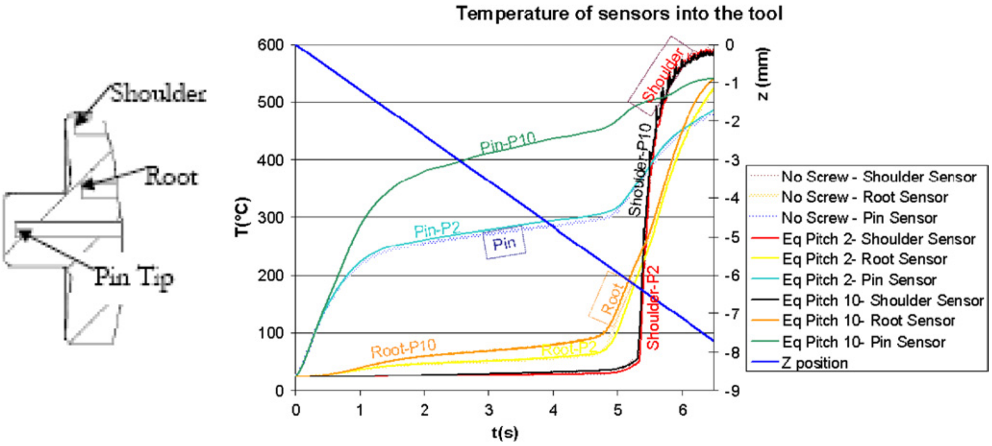

Figure 25. Right: location of the three thermal sensors in the tool at the probe, root and shoulder. Left: comparison of calculated temperatures (in °C) at these three locations during a 7 s plunge with unthreaded tool, 2 mm and 10 mm equivalent screw pitch.

shoulder than in the case without threads. This correlates well with the fact that the equivalent strain close to the top surface is lower in the case with threads (see figure 29).

Therefore, threads clearly facilitate the deposition process on the trailing bottom side of the probe, and their action is all the more necessary that the probe is longer, which is shown by

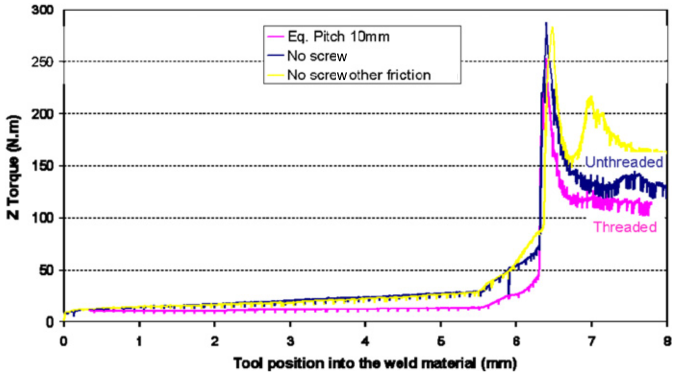

Figure 26. Comparison of torques during the plunge phase for the studied cases: unthreaded and threaded probe with a 10 mm equivalent pitch.

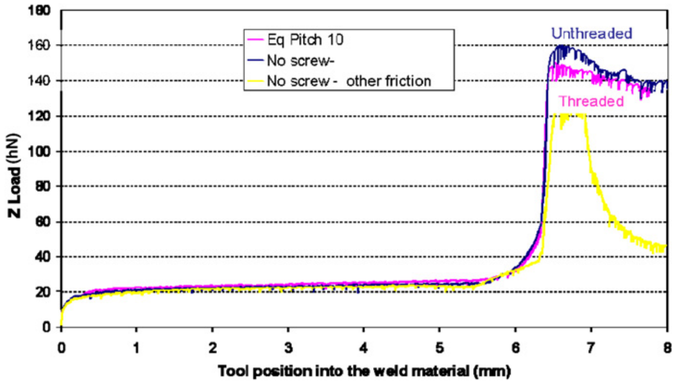

Figure 27. Comparison of vertical forces (hN) during the plunge phase for the studied cases: unthreaded and threaded probe with a 10 mm equivalent pitch.

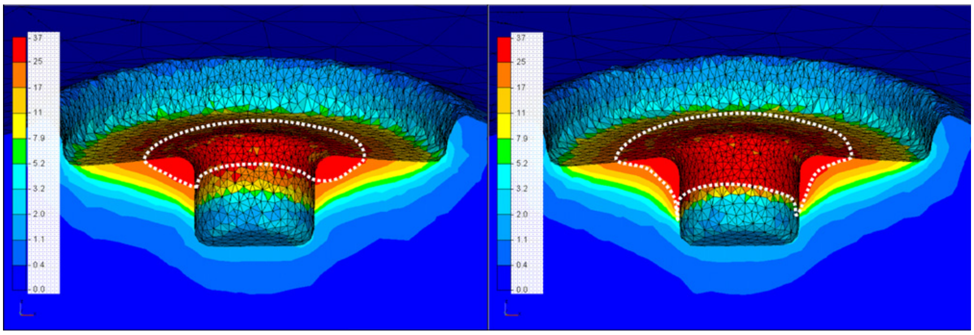

Figure 28. Comparison of the equivalent strain maps in the cross section after a 7 s plunge for unthreaded (right) and threaded (left) probe with a 10 mm equivalent pitch.

carrying out another simulation on a longer probe of 10.16 mm length and a 10 mm equivalent screw pitch. In this case, only the threaded probe has provided a successful weld, while voids occurred with a smooth probe. Figure 31 shows how the action of the threads leads to a good deposition process, even though the contact is still not perfect with some of the nodes losing the contact with the trailing bottom side of the probe.

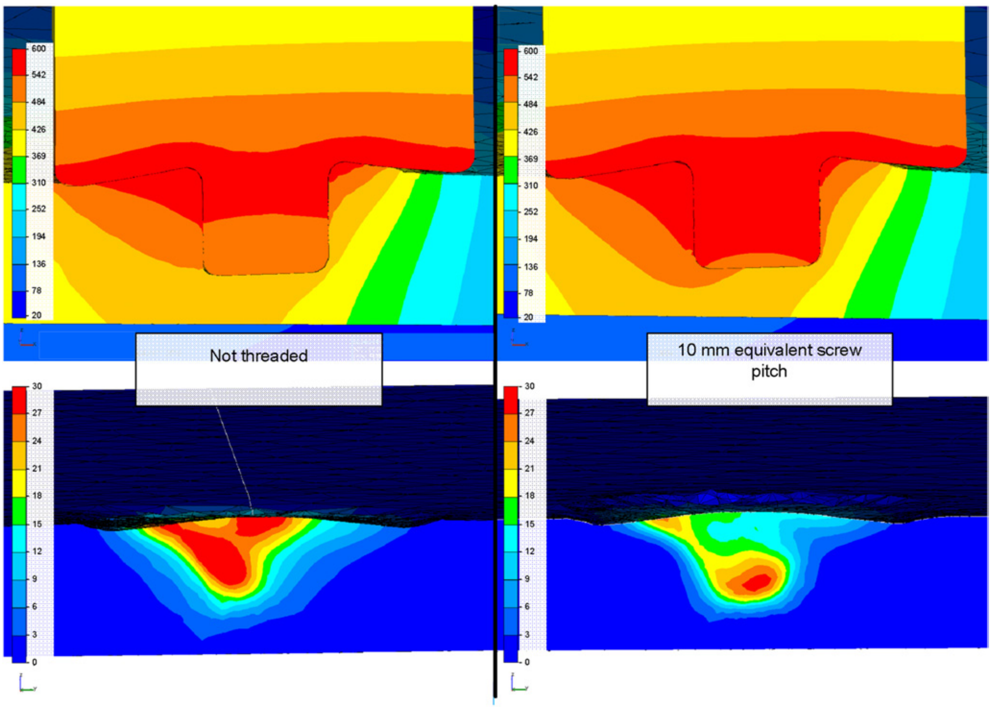

Figure 29. Comparison of the ALE welding phase with threaded and unthreaded probe tools. Top: temperature (in °C) after 21 s of welding (cross joint section view). Bottom: equivalent strain at the back of the probe.

As the microstructure evolution of aluminium is dominated by dynamic recrystallization at such elevated temperatures [29], which is itself mainly governed by the material deformation, the grain size gradients provide good indications about the strain gradients. For such a long probe, a double nugget is experimentally observed under such welding conditions, as can be seen in the micrograph of figure 32. Its numerical modelling would require much finer meshes than the ones used in the simulation. However, the equivalent strain isovalues in a transverse cross section just behind the probe (see figure 32) show an increase in the nugget size (see figure 29 for comparison).

6.3. Convex tool

The shoulder of the tool, which is regarded as the main source of heat generation, is concave in shape, which was thought to aid in weld consolidation by forcing the softened material to remain in the welding zone as the tool moves along the joint line. Other tool designs are also quite popular and might be better suited for other materials. Figure 33 shows such a convex tool: it has a conical threaded probe and a convex threaded shoulder, which allow welding without tilting the spindle.

In order to better understand the role of these threads, two simulations have been run, with threaded and unthreaded tools. The welding and material parameters are kept the same, as in the previous welding simulations. Threads are modelled as before by an additional virtual velocity, which is tangent to the tool surface and oriented perpendicular to the experimental

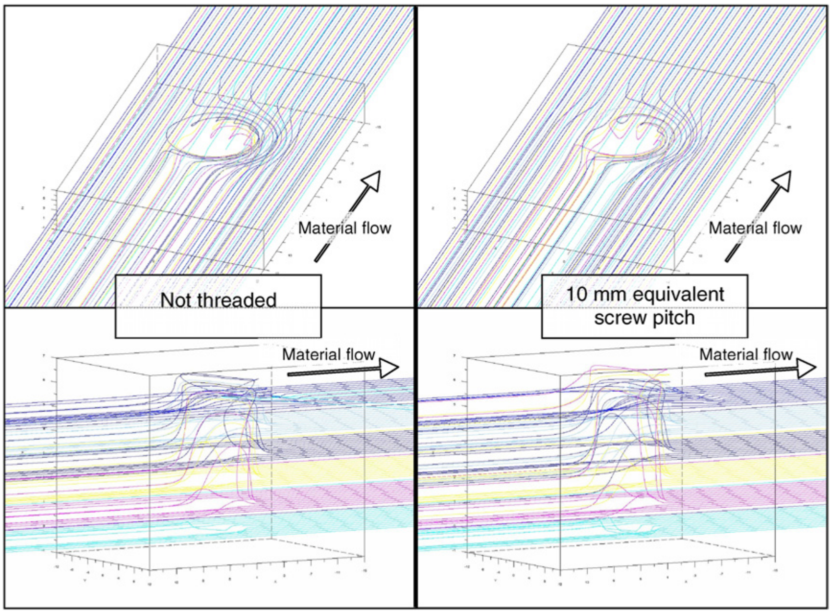

Figure 30. Comparison of computed stream lines with and without threads (the stream lines are regular at the outflow and constructed backwards through the flow field).

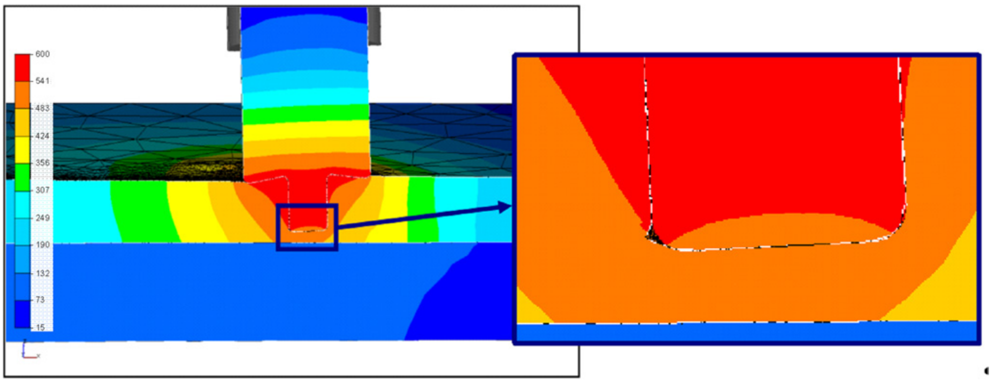

Figure 31. Temperature map (cross section view, °C) after 12 s of an ALE welding simulation of a 10.16 mm probe. The contact is lost for some of the nodes at the bottom trailing side of the probe while the action of threads is simulated through a 10 mm equivalent screw pitch.

threads. This virtual velocity is taken into account for all the nodes which are in contact not only with the probe but also with the shoulder, as illustrated in figure 33.

With the smooth tool, the simulation rapidly stops: a void appears at the trailing advancing side of the probe. Figure 34 shows the initial contact area for the two simulations, the loss of contact which immediately occurs with the unthreaded tool and the 'foot print' of the tool after 17 s of welding with the threaded tool (no void is generated).

Figure 35 shows the stream lines and the equivalent strain observed in a cutting transverse plane located just behind the probe. The temperature field resulting from the simulation is shown in figure 36.

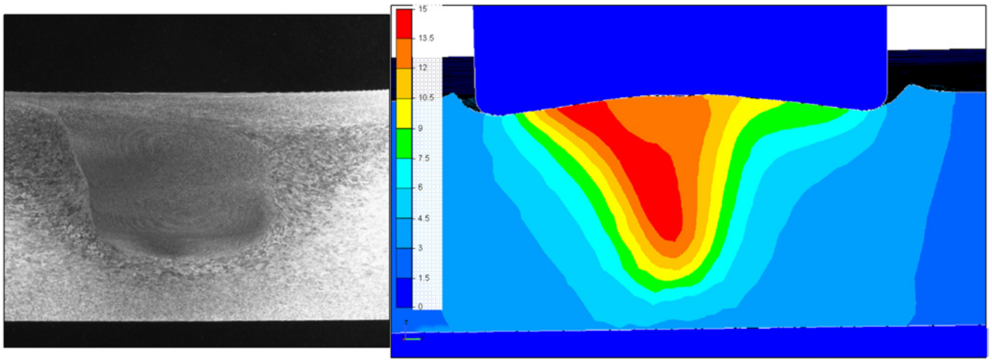

Figure 32. Comparison of experimental transverse cut and simulated equivalent strain in a transverse cutting plane at the back of the probe.

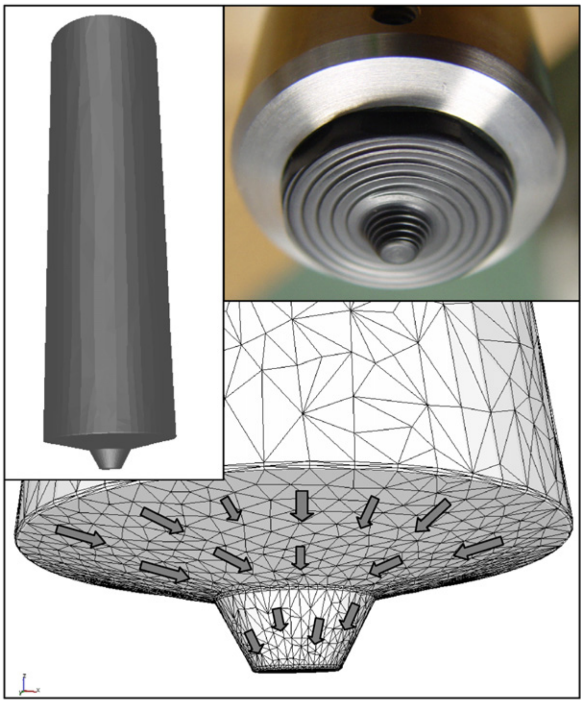

Figure 33. Convex tool shape: experimental tool (on top right) and modelled one; the arrows illustrate the added virtual velocities for threads modelling.

All these results mainly show the feasibility of the numerical simulation with a very different kind of tool design, as well as the type of information that can be provided for tool design.

7. Conclusions

A numerical tool that allows computing the thermo-mechanical fields during all phases of FSW without any hypothesis or supplementary information about the process, just by relying

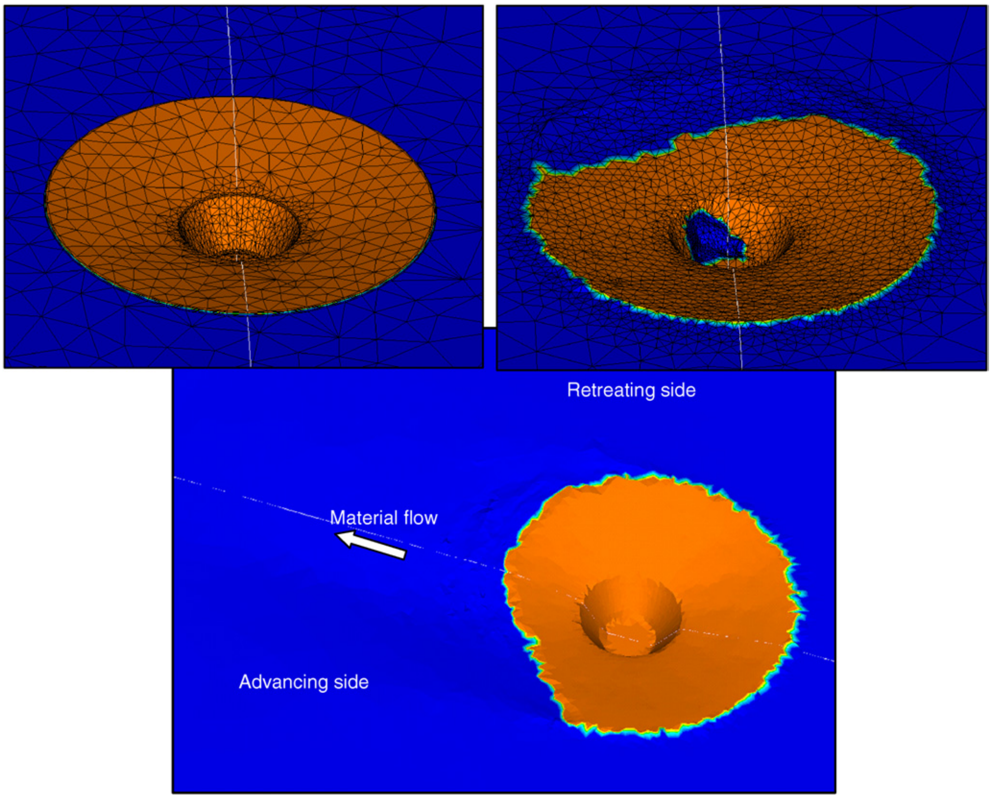

Figure 34. ‘Foot prints’—contact areas: blue nodes are not in contact with the tool. Top left: at the beginning; top right: after 2 s with the smooth tool; bottom: after 17 s of welding simulation with the threaded tool.

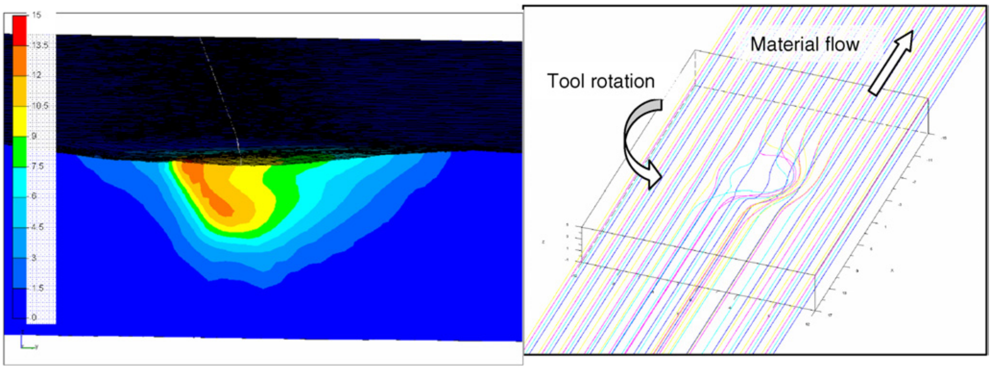

Figure 35. Left: equivalent strain in a transverse cross section at the back of the probe. Right: material stream lines computed after 17 s of welding (the stream lines are regular at the outflow and constructed backwards through the flow field).

on accurate constitutive and friction models, was developed. The master key of the numerical approach is an accurate modelling of the unilateral contact conditions between the plate and the tool. It allows precise computing of the contact area and modelling of the various contact instabilities that may occur during the process, and to avoid making any hypothesis or inverse

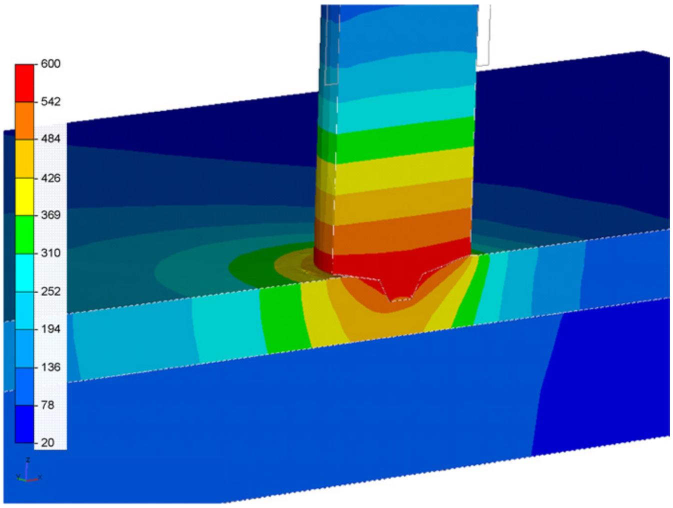

Figure 36. Temperature map (in °C) in the cross joint section and after 17 s of welding.

analysis to determine it. The presented welding applications show how different the results can be, in terms of forces and torques, depending on whether the contact area is regarded as fixed or is allowed to change during the process. The adaptive ALE formulation makes it possible to simulate the different non-steady phases of the FSW process as well as the steady welding phase, using an elasto-viscoplastic constitutive model that is favourable to residual stress calculations. Preliminary comparisons between simulations and experimental results show that this numerical model is able to reproduce the main phenomena observed in FSW: it provides the good tendencies, the right sensitivities and good agreements on the welding forces. It succeeds in reproducing most of the features of the FSW process, such as the role played by the plunge depth of the tool on the plate and its effect on the formation of flashes, the slight cooling that occurs during the dwelling when the vertical welding force is not controlled, the possible formation of non-steady voids or tunnel holes, and the influence of threads on the material flow, the contact zone, the temperature field and the welding efforts.

This numerical tool has the capacity to aid in finding the thermo-mechanical conditions that are favourable for a proper deposition process, and in adjusting the process parameters to avoid void formation, which can be suggested as a preliminary criterion for evaluating the success of a weld. It makes it possible to analyse the influence of the probe length, of the threads pitch, of the tool shape and concavity, and can so be utilized in tool design. It allows studying the plunging step in detail and can consequently be extended to the analysis of friction stir spot welding for joining similar or dissimilar plates.

This paper mainly demonstrates the capacities of a 3D numerical model to accurately simulate most types of material flows that are encountered in FSW, and to accurately compute the resulting thermo-mechanical fields. However, this process being very highly coupled, these calculations highly depend on proper selections of constitutive and frictional models, as well as interface coefficients. Unfortunately, such models do not fully exist today, according to the complexity of the material solicitations in terms of strains, strain rates and temperature gradients. Therefore, further investigations are necessary to evaluate whether rather simple material and frictional models, such as the ones used in this paper, are enough to provide predictive software, or whether more complex models should be investigated. This requires more comparisons with experiments, in terms of forces, torques, temperatures and metallurgy. In section 3 of this paper, it was noticed how sensitive the results can be to small variations of the friction coefficient, so more work is particularly required to properly identify the friction coefficients and validate the calculated thermal profiles.

Acknowledgments

Support for this work has been provided by the Office of Naval Research under contract N00014-03-1-0792, Dr Julie Christodoulou, Program Manager.

References

[1] Russell M J, Shercliff H R and Threadgill P L 2001 Development and application of an analytical process model for friction stir welding *Aluminum 2001: Proc. of the TMS Annual Meeting (New Orleans, LA, USA)* ed S K Das and J Kaufman pp 225–34

[2] McClure J C, Tang W, Murr L E, Guo X, Feng Z and Gould J E 1998 A thermal model of friction stir welding *Trends in Welding Research Conference (Pine Mountain, GA, USA)* pp 590–5

[3] Feng Z, Gould J E and Lienert T J 1998 A heat flow model for friction stir welding of aluminum alloys *2nd Symp. on Hot Deformation of Aluminum Alloys (Rosemont, IL, USA)* pp 149–58

[4] Gould J E and Feng Z 1999 Heat flow model for friction stir welding of aluminum alloys *J. Mater. Process. Manuf. Sci.* **7** 185–94

[5] Schmidt H, Hattel J and Wert J 2004 An analytical model for the heat generation in friction stir welding *Modelling Simul. Mater. Sci. Eng.* **12** 143–57

[6] Khandkar M Z H, Khan J A and Reynolds A P 2003 Input torque based thermal model of friction stir welding of Al-6061 *Trends in Welding Research (Probee Mountain, GA, USA)* pp 218–23

[7] Chen C M and Kovacevic R 2003 Finite element modeling of friction stir welding-thermal and thermomechanical analysis *Int. J. Mach. Tools Manuf.* **43** 1319–26

[8] Lawrjaniec D, Abisror A, Decker C, Kocak M and Dos Santos J 2003 Numerical simulation of friction stir welding *Processing and Manufacturing of Advanced Materials (Madrid, Spain)* pp 2993–8

[9] Seidel T U and Reynolds A P 2003 Two-dimensional friction stir welding process model based on fluid mechanics *Sci. Technol. Weld. Join.* **8** 175–83

[10] Chao Y J, Qi X and Tang W 2003 Heat transfer in friction stir welding: experimental and numerical studies *J. Manuf. Sci. Eng.* **125** 138–45

[11] Ulysse P 2002 Three-dimensional modeling of the friction stir-welding process *Int. J. Mach. Tools Manuf.* **42** 1549–57

[12] Long T, Seidel T U, Tang W and Reynolds AP 2003 A friction stir welding model using computational fluid dynamics *3rd Symp. on Hot Deformation of Aluminum Alloys (San Diego, CA, USA)* pp 299–312

[13] Colegrove P A and Shercliff H R 2003 Experimental and numerical analysis of aluminium alloy 7075-T7351 friction stir welds *Sci. Technol. Weld. Join.* **8** 360–8

[14] Colegrove P A, Shercliff H R and Threadgill P L 2003 Modelling and development of the Trivex Friction Stir Welding Tool *4th Int. Symp. on Friction Stir Welding (Park City, UT, USA)*

[15] Cho J H, Boyce D and Dawson P 2007 Modelling of strain hardening during friction stir welding of stainless steel *Modelling Simul. Mater. Sci. Eng.* **15** 469–86

[16] Xu S, Reynolds A P and Seidel T U 2001 Finite element simulation of material flow in friction stir welding *Sci. Technol. Weld. Join.* **6** 191–3

[17] Schmidt H and Hattel J 2005 A local model for the thermomechanical conditions in friction stir welding *Modelling Simul. Mater. Sci. Eng.* **13** 77–93

[18] Buffa G and Fratini L 2004 Friction stir welding of AA6082-T6 sheets: numerical analysis and experimental tests *8th NUMIFORM Conference (Columbus, OH, USA)* pp 1224–9

[19] Fratini L and Buffa G 2005 CDRX modelling in friction stir welding of aluminium alloys *Int. J. Mach. Tools Manuf.* **45** 1188–94

[20] Coupez T, Soyris N and Chenot J L 1991 3-D finite element modelling of the forging process with automatic remeshing *J. Mater. Process. Technol.* **27** 119–33

[21] Chenot J L and Fourment L 2002 Finite element simulation of the forging process: future developments *5th ESAFORM Conference (Krakow, Poland)* ed M Pietrzyk and Z Mitura (Krakow, Poland: Akapit)

[22] Bellet M and Fachinotti V 2004 ALE method for solidification modelling *Comput. Methods Appl. Mech. Eng.* **193** 4355–81

[23] Fourment L and Guerdoux S 2006 Enhanced transport and remeshing schemes for ALE formulations: application to numerical simulation of friction stir welding *9th ESAFORM Conference (Glasgow, UK)* (Krakow, Poland: Akapit) pp 75–8

[24] Guerdoux S and Fourment L 2007 Error estimation and accurate mapping based ALE formulation for 3D simulation of friction stir welding *NUMIFORM 07—Materials Processing and Design: Modeling, Simulation and Applications (Porto, Portugal)* ed J M A César de Sà and A D Santos (New York: AIP) pp 185–90

[25] Boroomand B and Zienkiewicz O C 1997 Recovery by equilibrium in patches (REP) *Int. J. Numer. Methods Eng.* **40** 137–64

[26] Boussetta R, Coupez T and Fourment L 2006 Adaptive remeshing based on a posteriori error estimation for forging simulation *Comput. Methods Appl. Mech. Eng.* **195** 6626–45

[27] Zienkiewicz O C and Zhu J Z 1992 The superconvergent patch recovery (SPR) and adaptive finite element refinement *Comput. Methods Appl. Mech. Eng.* **101** 207–24

[28] Liszka T and Orkisz J 1980 The finite difference method at arbitrary irregular grids and its application in applied mechanics *Comput. Struct.* **11** 83–95

[29] Gourdet S and Montheillet F 2003 A model of continuous dynamic recrystallization *Acta Mater.* **51** 2685–99